FINAL REPORT

Integration of Multi-Tension Permeametry and Photogrammetric Textural Segmentation for Estimating Directional Permeability

SERDP Project ER-1366

April 2010

Anderson Ward
Pacific Northwest National Laboratory

Gamal Seedahmend
University of Florida

Greg Anderson
SPAWAR Systems Center

Fred Zhang
Pacific Northwest National Laboratory

DISCLAIMER

PACIFIC NORTHWEST NATIONAL LABORATORY
operated by
BATTELLE
for the
UNITED STATES DEPARTMENT OF ENERGY
under Contract DE-AC05-76RL01830

Printed in the United States of America

**Available to DOE and DOE contractors from the
Office of Scientific and Technical Information, P.O. Box 62, Oak Ridge, TN 37831;
prices available from (615) 576-8401.**

**Available to the public from the National Technical Information Service,
U.S. Department of Commerce, 5285 Port Royal Rd., Springfield, VA 22161**

Table of Contents

page

List of Figures

List of Tables

Acronyms

CCD	Charge Couple Device
CPT	Cone Penetrometer Technology
DOD	U.S. Department of Defense
DOE	U.S. Department of Energy
EPA	U.S. Environmental Protection Agency
FOV	Field of View
LED	Light Emitting Diode
PNNL	Pacific Northwest National Laboratory, Richland, WA
PSD	Particle size distribution
PV	Pixel-Vernier
SCAPS	Site Characterization and Analysis Penetrometer System
SERDP	Strategic Environmental Research and Development Program
SPAWAR	Space and Naval Warfare Systems Center, San Diego, CA

Acknowledgments

This work was funded by the Strategic Environmental Research and Development Program (SERDP) under Contract Number DE-AC06-76RL01830, as Cleanup Program #1366. The SERDP Program Manager for CU-1366 was Dr. Andrea Leeson. The Department of Energy (DoE) Technical Liaison for this work was Ms. Beth Moore.

Design work related to the camera systems and incorporating photogrammetric software into the operating system of the Site Characterization and Analysis Penetrometer System (SCAPS) was conducted at the Space and Naval Warfare Systems Center (SPAWAR) by Dr. Greg Anderson. The development of property transfer models relating hydraulic properties to particle size distributions and photogrammetric methods, including software development were conducted at Pacific Northwest National Laboratory (PNNL) by Dr. Andy Ward, and Dr. Gamal Seedahmed (now at the University of Florida).

Lastly, we acknowledge student interns Mr. LaShane Carter, Mr. Bruce Johnson, Miss. Kaetochi Okembgo, and Mr. Ameer Tillman; Mr. Jason Keller (formerly of PNNL) who assisted in data collection and analysis with the borehole permeameter system; and Mr. Tao Fu (PNNL) who assisted in the testing of photogrammetric tools following the departure of Dr. Seedahmed from PNNL in 2007.

Executive Summary

The Pacific Northwest National Laboratory (PNNL), in collaboration with The Space and Naval Warfare Systems Center (SPAWAR) proposed to develop a rapid, robust and reliable tool for in situ measurement of hydraulic properties in heterogeneous, anisotropic, variably saturated porous media. A critical component of this project was the modification of the existing SCAPS/GeoVIS system to function as dual field-of-view video camera system for sub-surface soil imaging. This required modification of the single-camera GeoVis system to allow simultaneous capturing of images at different magnification factors to allow a more complete description of the grain size distribution curve. One camera is used to capture grain size data in the silt-sized fraction and the other to capture information in the sand-sized fraction. These two levels of magnification provide fields of view ranging from 2 to 20 mm diagonal.

Digital images of sediments were converted into particle size distributions and their moments using the Pixel-Vernier, a suite of photogrammetric algorithms that combine markers-controlled watershed algorithm with a minimum-distance clustering to solve the segmentation problem. The segmentation algorithm decomposes the image into separate particle regions, which are used to derive several geometric attributes for each particle. These were used to estimate the particle size distribution and their relevant statistics. Particle size distributions were then used with a packing model to estimate porosity and saturated hydraulic conductivity which have the added benefit of constraining hydraulic conductivities derived from the borehole permeameter measurements. The approach proved successful in characterizing a diverse set of materials such as including soil, complex digital patterns, and sediment images from the Mars surface.

In laboratory tests to calibrate the instruments and models, sediments were separated in 1ϕ fractions and characterized to determine particle shape, porosity and hydraulic conductivity. Binary mixtures of coarse and fine fractions were prepared with the fine fraction ranging from 0 to 100%. Measurements of particle shape, porosity and hydraulic conductivity were made on end members and mixtures. Results show that particles in all size classes are aspherical and that end-member porosity increases with decreasing particle diameter in the sand fraction and smaller. In the gravel fraction, end-member porosity initially increased with increasing diameter before becoming constant. A model for the incomplete mixing of aspherical particles proved successful in predicting porosities and conductivities. Both parameters decreased to a minimum at a critical fines content confirming the importance of knowing the fractional concentrations of each component.

A subatmospheric borehole permeameter proved successful in overcoming limitations in subsurface conductivity measurements. Use of a subatmospheric pressure permeameter reduced the effect of macropores and fissures on matrix flow. For the analysis of data, a new method using the Brooks-Corey hydraulic model was developed to solve the steady-state infiltration equation. Results from numerical simulations compared well with laboratory experiments. Field measurements were also in good agreement with independent measurements although the saturated hydraulic conductivity was slightly underestimated. With the successful application of the packing model to the prediction of porosity and saturated hydraulic conductivity, the saturated hydraulic conductivity can be easily constrained in the permeameter analysis.

This approach will lead to a better understanding of the measurements available for permeability characterization and help to establish the validity of permeability predictions in untested intervals based on measurements like grain size distributions that are easier to make. The data obtained using the direct push sensors will be invaluable in the design and evaluation of remedial systems and the prediction of future contaminant migration.

1. Objectives

The SERDP Cleanup Statement of need, CUSON-04-01, entitled "Innovative and low-cost methods for measuring hydraulic conductivity" was aimed at identifying improved or new technologies and procedures for in situ measurement of permeability. In response to this need, the Pacific Northwest National Laboratory (PNNL) proposed an integrated characterization approach that would provide estimates of *in situ* hydraulic properties from the scale of laminae up to the formation scale. The principle objective of the proposed work was to develop a rapid, robust and reliable tool for in situ measurement of hydraulic properties in heterogeneous, anisotropic, variably saturated porous media. To meet the overall objective, a number of technical objectives were identified, including:

- development a borehole permeameter module for measuring hydraulic properties
- development of a dual-camera imaging system for in-situ grain size images
- development of photogrammetric algorithms to determine grain-size distributions from downhole video images

The different components would ultimately be integrated into a single multipurpose tool for deployment using direct push technology. The proposed work was expected to provide a means for estimating *in situ* hydraulic properties from downhole measurements.

To obtain the data necessary to meet the specific objectives listed above, a combination of numerical, laboratory, and field studies were designed and implemented to characterize properties sediments and relate these properties back to those that could be easily measured with direct push technology. A team of researchers was assembled to develop direct push, *in situ* sensors that could be deployed individually or as part of an integrated tool. The sensors included: 1) a tension (subatmospheric pressure) permeameter for measuring variably relative permeability as a function of saturation, and 2) a microscopic imaging system for *in situ* imaging of sediments from which grain-size characteristics and independent estimates of hydraulic properties would be derived using digital photogrammetry.

This report represents the two-year final progress report for SERDP project CU-1366 entitled "The Integration of Multi-Tension Probe Permeametry, and Digital Photogrammetry for the Improved Characterization of Subsurface Permeability" for the period 2005 to 2007. This project was a collaborative effort between the Pacific Northwest National Laboratory (Dr. Andy Ward, Dr. Gamal Seedahmeed) and the Space and Naval Warfare Systems Center (Dr. Greg Anderson).

2. Background

The occurrence and impact of spatial variability in hydrogeologic properties of natural soils and sediments is well established. Soil-forming processes typically result in structures whose properties vary with: 1) the scale of observation, 2) space (heterogeneity), and 3) and orientation (anisotropy). Differences in space and orientation can lead to complex variations in hydrologic properties, manifested as heterogeneity, that strongly affect the distribution of contaminants in the subsurface. Thus, predictions of contaminant fate and transport; design of remedial systems; and evaluation of the effectiveness of remediation schemes are also hampered by the multi-scale heterogeneity. More specific to this work is the impact of heterogeneity on the ability to characterize hydraulic properties at the scales controlling transport.

As a result of subsurface heterogeneity, there is a discrepancy in parameters parameter values at the scale at which measurements are typically made and the scale at which input data are needed for models used for interpretation and prediction. For example, Figure 1 shows a typical cutface from the uppermost sedimentary unit of the Hanford Formation where a significant portion of vadose zone contaminants resides. This particular sedimentary unit consists of glacio-fluvial sediments with heterogeneities ranging from localized ripples to horizontal intercalations of silt and gravel lenses. These sediments are characterized by discrete bedding planes and other abrupt structural features, rather than a smoothly varying structure. This type of heterogeneity is typical of natural soils and sediments can result in contrasts in hydraulic properties that lead to complex behavior of fluids and contaminants in these systems. In fact, it is characterized by several disparate length scales that in many cases prohibit the use of effective or average parameters for predicting transport (Russo et al. 2001).

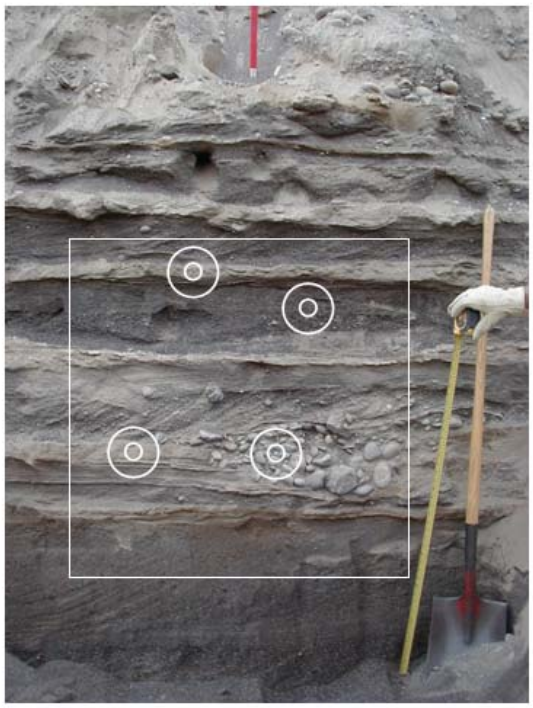

Figure 1. Exposed Trench Face Showing Layered Heterogeneity in Hanford's 200 Area showing typical 1×1-m model grid block (white square) used for numerical simulations relative to the typical 5-cm and 15-cm sediment cores (white circles) used for characterizing sediment properties.

Characterizing this heterogeneity, for the purpose of predicting water flow and reactive transport behavior at the field scale, has proven quite difficult. This difficulty is directly related to the disparities in the scales at which transport processes occur, the scales at which measurements are typically made, and the scales at which models are applied (Figure 1). These features represent two main challenges to parameterization: 1) how best to account for the effects of the multi-

scale heterogeneity on transport properties, and 2) identifying the sufficiency of data required to adequately describe these properties. Ideally, the modeler wants to describe the global behavior while keeping the local-scale behavior as close to reality as possible. However, the identifying, parameterizing and represent ting the small-scale features remains a challenge when trying to interpret or predict large-scale transport behavior.

One solution to this dilemma is to merge information from various measurement scales obtained at the same location and then determine the effect of heterogeneity patterns on large-scale prediction of transport in porous media. The problem is that there is no single integrated tool that allows convenient and cost-effective measurement of hydraulic properties at multiple scales without destroying the structure of the sediment. The hydraulic properties of interest include hydraulic conductivity as a function of saturation, K(S); capillary pressure as a function of saturation, h(S); porosity (ϕ); residual saturation, S_r; and the parameters describing pore morphology and connectivity. These parameters are required as input for quantitative models used in remedial system design and evaluation and for predicting contaminant fate and transport.

As shown in Figure 1, heterogeneity typically manifests across several spatial scales causing transport to be impacted simultaneously by high-permeability materials and low-permeability lenses. Yet, typical measurements of K(S) and h(S) tend to smooth out the effects of local-scale heterogeneities and the associated anisotropy, which are known to dominate subsurface flow and transport processes. The omission of heterogeneity at or below the scale of measurement of the typical permeameter generates a permeability field that ignores the effects of fine-scale lamination and underestimates variability. Thus, the resulting picture is often insufficient for: 1) adequate interpretation of contaminant distributions, 2) optimized remedial system design, or 3) prediction of future fate and transport.

2.1 Technical Approach

To obtain the data necessary to meet the specific objectives listed above, a combination of numerical, laboratory, and field studies were designed and implemented to characterize sediment properties and establish relationships to grain size distributions that would be derived from down-hole images and in situ permeability estimates. The numerical component of the research was designed to analyze digital images and derive parameters known to influence particle packing and ultimately soil physical and hydraulic properties. The laboratory component of the research was aimed at characterizing select sediments to establish end member behaviors of different sediment size classes (porosity, permeability) and model mixtures of these end members and to test new instrumentation. The field component was designed to test the instrumentation and analytical methods under field conditions.

The tasks completed as part of this project are summarized herein and discussed in more detail in the following sections.

Task 1: Development of a borehole permeameter module to measure hydraulic conductivity at sub-atmospheric and atmospheric pressures. This module included sensors for measuring the permeameter outflow rate and matric potential (soil water pressure) at the outlet and at offset points in response injections at different inlet pressure heads.

Task 2: Development of a dual-camera, microscopic imaging system for *in-situ* digital imaging of the porous medium at the sub-millimeter scale.

Task 3: Development of photogrammetric algorithms to automatically segment digital images into facies based on grain size statistics (mean diameter and sorting index). The resulting grain size distributions, geometric mean grain diameter, grain size variance, eccentricity, and mean particle orientation are used in the estimate of porosity and hydraulic conductivity.

Task 4: Field testing of the integrated system at the Hanford Site, in collaboration with Hanford's Science and Technology Vadose Zone-Groundwater Integration Project. Tests were not performed at Hanford as the Science and Technology Project had come to an end prior to completion of this work. Tests were completed in San Diego at the SPAWAR facility.

3. Materials and Methods

3.1 Task 1: Borehole Permeameter for Hydraulic Conductivity

It well recognized that *in situ* estimates of hydraulic properties better represent field conditions than laboratory measurements on repacked or undisturbed cores. Methods commonly used to estimate permeability include pneumatic and hydraulic slug tests with permeameters deployed by cone penetrometer and hollow-stem augers, dynamic formation testers, and borehole electrical imaging devices (Chandler et al., 1989; Lowry et al., 1999; Gribb et al. 2000; Sorensen et al, 2001; Morton et al, 2002) and acoustic techniques using Stonely waves (Paillet et al., 1992). Many of these techniques have proven capable of producing large amounts of data, some of which have been used to predict hydraulic conductivity in unsampled locations based on correlations with other geophysical measurements. However, rigid sampling procedures often omit important permeability features from the sampling program (Thomas et al., 1997) resulting in the underestimation of spatial variability in conductivity. Neglecting heterogeneity below the scale of measurement of the typical permeameter results in conductivity estimates that may not reflect the effects of fine-scale lamination and underestimate the effects of variability.

In situ methods for hydraulic properties have been developed for vadose zone measurement, particularly in the agricultural arena, and have been focused on near-surface measurements. Measurement techniques include tension infiltrometer, pressure infiltrometers, and borehole permeameters (e.g., Clothier and White, 1981; White and Sully, 1987; Smettem and Clothier, 1989; Reynolds and Elrick, 1990a,b; Hussen and Warrick, 1993; Zhang, 1997). Borehole permeameters like the Guelph Permeameter have long been used to measure subsurface unsaturated hydraulic properties but most use positive pressure heads (e.g., Reynolds et al., 1985; Amoozegar, 1989). In highly fissured geologic formations and soils with substantial amounts of macropores, maintaining a positive pressure in the borehole or cavity is virtually impossible and estimates of permeability are biased by the presence of preferential pathways (Wu et al., 1993).

A viable solution to this problem is to supply water under tension using an inflatable borehole tension permeameter (Or et al. 2000). Use of a subatmospheric pressure permeameter would reduce the effect of macropores and fissures on matrix flow. However, designs proposed thus far cannot be used to determine hydraulic conductivity at low (more negative) matric potentials. Present analysis of data from these measurements is based on the assumption of a 'linear' soil in which the logarithm of K varies linearly with the logarithm of pressure head. Such soils may be described by an analytical solution to the steady flow from cavities that assume a simple exponential representation of the unsaturated hydraulic function (Gardner, 1958). However, such an analysis has been shown to be applicable only to coarse-textured soils and sediments.

The objectives of this task were to develop a more robust design of borehole permeameter for use in heterogeneous sediments, to establish a more generalized approach for analyzing the steady-state infiltration rates, to develop an appropriate theory to describe the behavior of the permeameter and to facilitate optimization of its design by numerical modeling. To meet these objectives, we developed a rigid wall permeameter to measure outflow rates. For the analysis of data, a new method using the Brooks and Corey (1964) hydraulic model was developed for the

solution of the steady-state infiltration equation. Results from numerical simulations were compared with the results of laboratory experiments.

The soil hydraulic property that controls flow into unsaturated soil from a borehole tension permeameter is the relation between the unsaturated hydraulic conductivity *K* and capillary pressure head ψ. The integral of the K(ψ) relationship, know mathematically as the Kirchoff transform, has been shown by Gardner (1958) and others to be particularly useful for describing soil water flow:

$$\phi(\psi) = \int_{\psi_0}^{\psi} K(\zeta)d\zeta \tag{1}$$

where ϕ(ψ) is known as the flux potential (Gardner, 1958), ζ is the variable of integration, ψ_0 is some arbitrarily chosen constant (usually the initial water potential) but the upper integration limit, ψ, is variable. Elrick and Reynolds (1992) further defined several specific values of ϕ(ψ) for fixed upper limits of integration defined in Equations 2 through 5 below. The residual flux potential is given by

$$\phi_r = \int_{-\infty}^{\psi_i} K(\zeta)d\zeta; \quad -\infty < \psi_i \le 0 \tag{2}$$

where ψ_i is initial pressure head. The tension flux potential is given by

$$\phi_t(\psi) = \int_{-\infty}^{\psi} K(\zeta)d\zeta; \quad \psi_i < \psi_t \le 0 \tag{3}$$

Similarly, the matric flux potential is given by

$$\phi_m = \int_{-\infty}^{0} K(\zeta)d\zeta; \quad \psi_i \le 0 \tag{4}$$

whereas the velocity flux potential is given by

$$\phi_v = \int_{0}^{H} K(\zeta)d\zeta = K_s H; \quad H > 0 \tag{5}$$

where H is a positive pressure head. For most field soils at field capacity or drier, ϕ_r is negligibly small and can be ignored.

The ϕ_t values represent the component of ϕ(ψ) that is appropriate for a tension permeameter supplying water to the infiltration surface at the negative potential, ϕ_t. The ϕ_m and ϕ_v values are the appropriate components of ϕ(ψ) for a pressure permeameter where water is supplied to the infiltration surface under the positive head, H. The steady-state flow of water from a borehole permeameter can be described by equations of the form (Reynolds et al., 1985; Philip, 1987; Reynolds and Elrick, 1990, 1991),

$$Q = Q_g + Q_m + Q_v$$
$$= \pi a^2 K_{fs} + \frac{2\pi H}{C}\phi_m + \frac{2\pi H}{C}\phi_v \quad (6)$$

where Q is the steady flow rate of water into the soil and Q_g, Q_m, and Q_v are the components due to gravity, capillarity, and pressure, respectively; a is the radius of the borehole permeameter; C [-] is the well shape factor that is a function of H/a and can be determined by a chart (Reynolds, 1986; Soil Moisture Corp., 1987) or by empirical formula (Zhang et al., 1998) as given below for sand, loam or structured clay, and unstructured clay respectively:

$$C_1 = \left(\frac{H/a}{2.074 + 0.093\, H/a} \right)^{0.754} \quad (7)$$

$$C_2 = \left(\frac{H/a}{1.992 + 0.091 H/a} \right)^{0.683} \quad (8)$$

$$C_3 = \left(\frac{H/a}{2.102 + 0.0118 H/a} \right)^{0.655} \quad (9)$$

A borehole tension permeameter can therefore be used to determine unsaturated hydraulic conductivity at any desired matric potential. For convenience of using the log scale we define a soil water tension, h as -ψ. For flow rate from a borehole tension permeameter operating at tension, h, equation (6) can be modified to give:

$$Q(h) = \pi a^2 K(h) + \frac{2\pi H}{C}\phi_t(h) \quad (10)$$

There are a variety of models that can be used to describe soil hydraulic conductivity function, K(h). Here we choose the Gardner (1958) and the Brooks and Corey (1964) models for comparison owing to their ease of integration. Three alternate methods of analysis based on these two models are presented below.

3.1.1 Continuous Brooks and Corey Model. For more accurate description of K(h), the Brooks and Corey (1964) model maybe used:

$$K(h) = \begin{cases} K_s \left(\frac{h_e}{h} \right)^m & if\ h > h_e \\ K_s & if\ h \le \psi_e \end{cases} \quad (11)$$

where h_e is the air-entry tension and m is a constant. Substituting Eq. (11) into (3) results in

$$\phi_t(h) = \begin{cases} K\dfrac{h}{m-1} & if\ h > h_e \\ K_s\dfrac{h_e}{m-1} + K_s(h_e - h) & if\ h \le h_e \end{cases} \tag{12}$$

Because we are trying to measure the unsaturated hydraulic conductivity, K(h), only the case of $h > h_e$ will be considered. Then substituting $\phi_t(h)$ for $h > h_e$ from eq. (12) into (10) yields the follow equation:

$$Q(h) = \pi a^2 K(h) + \frac{2\pi H}{C}\frac{h}{m-1}K(h) \tag{13}$$

Rearranging Eq. (13) to solve for K(h) gives

$$K(h) = Q\left(\pi a^2 + \frac{2\pi H}{C}\frac{h}{m-1}\right)^{-1} \tag{14}$$

Equation (14) can be used to calculate the unsaturated hydraulic conductivity at any matric potential once m is known.

For the typical direct push hole, the borehlole diameter is quite small (e.g., a = 2.5 cm). Thus, when water is supplied under tension $h < h_e$, the flow through the bottom of the borehole due to gravity, the first term at the right hand side Eq. 13, is much smaller than that due to capillary, the second term at the right hand side of Eq. 13. By neglecting the gravity effect, Eq. (13) can be rewritten as:

$$Q(h) = \frac{2\pi H}{C}\frac{h}{m-1}K(h) \tag{15}$$

For the permeameter with an impermeable bottom, Eq. (15) is accurate. Combining Eqs. (11) and (15) yields:

$$\ln Q(h) = \ln\left(\frac{2\pi H K_s}{C(m-1)}h_c^m\right) + (m-1)\ln(h) \tag{16}$$

Hence the value of parameter m can be determined from Eq. (16) by linear regression. The unsaturated hydraulic conductivity can then be determined using Eq. (14). However, when $h < h_e$, Eq. (16) cannot be used and Method 2 must be applied.

3.1.2 Piece-Wise Brooks and Corey Model. In some cases, as will be shown in the Results section, the Brooks and Corey (1964) model cannot describe the full range of the hydraulic conductivity curve. Then, the relationship between *ln(Q)* and *ln(h)* is not linear. In this case, the *ln(Q)* and *ln(h)* relationship may be treated as piece-wise linear. In other words, the slope of *ln(Q)* vs. *ln(h)* in Eq. (16), m-1, is not a constant. The slope of the i^{th} linear segment can be calculated as:

$$(m-1)_i = \frac{\ln(Q_{i+1}) - \ln(Q_i)}{h_{i+1} - h_i} \tag{17}$$

3.1.3 Piece-wise Gardner Model. The Gardner (1958) model developed for linear soils cannot be used to describe the entire range of K(h). The analysis can be extended to the entire range by treating the original model as a piece-wise log-linear model. The Garnder (1958) model is described by

$$K_g(h) = K_s \exp(-\alpha h) \tag{18}$$

where subscript 'g' denotes for the Gardner's model and α [L^{-1}] is a parameter inversely proportional to the capillary length. Substituting Eq. 18 into Eq. 3 produces

$$\phi_{tg}(h) = \frac{K(h)}{\alpha} \tag{19}$$

Substituting Eq. (12) into Eq. (10) and rearranging gives:

$$K(h) = Q\left(\pi a^2 + \frac{2\pi H}{C\alpha}\right)^{-1} \tag{20}$$

By measuring *Q* at a given tension, h, *K(h)* can then be determined from Eq. (20) once α is known.

By treating the Gardner (1958) model as a piece-wise linear function, α becomes a function of h but α must still be determined. The α parameter can be determined by first substituting the Gardner (1958) model into Equation 20 and taking logarithm to get a linear relationship between *ln(Q)* and α:

$$\ln(Q) = \ln\left[K_s\left(\pi a^2 + \frac{2\pi H}{C\alpha}\right)\right] - \alpha h \tag{21}$$

The slope α of the i^{th} linear segment can be calculated by

$$\alpha_i = \frac{\ln(Q_{i+1}) - \ln(Q_i)}{h_i - h_{i+1}} \tag{22}$$

3.3 Task 2: Dual-camera Microscopic Imaging System

A number of attempts have been made to capture images of subsurface sediments for use in characterization. Perhaps one of the more successful attempts has been the GeoVIS sensor mounted on SPAWAR's Site Characterization and Analysis Penetrometer System (SCAPS). The GeoVIS probe uses a miniature charge couple device (CCD) color video camera and appropriate optics system to image an area approximately 2 mm x 3 mm through a sapphire window on a cone penetrometer probe. The soil at the window is illuminated using LEDs mounted inside the probe. In its original configuration, the CCD camera system generates output as an analog video signal that is transmitted to the surface where it is displayed in real-time on a video monitor. The analog video signal is fed into a frame-grabber card installed in a microcomputer, which writes the data to the hard drive. When the push is terminated, the data was then transferred onto a compact disk and the digital data is available for post-processing.

The SCAPS GeoVIS system is capable of continuously imaging the soil through a sapphire window as the probe is pushed into the ground by the hydraulic ram in the cone penetrometer vehicle. Video images are collected at the standard video rate of 30 frames/sec. The video probe is advanced into the ground at push rates that range from approximately 0.169 to 0.5 cm/s (4 to 12 inches/min) depending on the optical magnification factor. Even at the fastest push rate of 0.5 cm/s (12 inches/min), an image is collected every 0.2 mm as the probe is advanced. Because the imaged area is approximately 2 mm × 3 mm, the video data appears as a continuous profile as the probe is pushed into the ground.

In its current configuration, there are four major technical limitations to using the GeoVis data for granulometry. First, the push rate is determined by the magnification factor and the resulting 0.169 to 0.5 cm/s rate is much slower than the standard CPT push rate of 2 cm/s. Second, although the mean grain diameter of most sediments typically range over several orders of magnitude (2 μm for clay, 25 μm for silt, and 2000 μm for sand) while the current system can resolve objects no smaller than 20 microns. Third, an image-based grain size distribution requires a statistically representative area of the soil specimen to be imaged in the field of view. However, the inverse relationship between field of view and magnification factor creates a major problem in effectively covering the range of grain sizes. If the magnification is too large, the large features will span multiple fields of view. Conversely, if the magnification is too small, smaller particles would be missed. Thus, the field of view of 3.6 mm diagonal may limit the sampling of a representative elementary area from which to calculate grain size distributions may not be sampled.

The objective of this task was to develop a dual field-of-view (FOV) video camera system for sub-surface soil imaging. This required modification of the single-camera GeoVis system to allow simultaneous viewing of the image at different magnification factors so as to capture the entire size distribution. At each magnification factor, image-based grain size analysis would be limited to those features that fall within predetermined limits. Since the complete particle size distribution can be predicted from information on the sand fraction and a single point in the fine textured fraction (Hwang et al, 2002), the modification would add a second camera to allow measurements at two levels of magnification. One camera would be used to capture grain size data in the silt-sized fraction ($2 \leq d \leq 63$ μm) and the second to capture information in the sand-sized fraction ($63 \leq d \leq 2000$ μm). These two levels of magnification would provide fields of view ranging from 2 to 20 mm diagonal. In addition, the light source would be modified to use a strobe light source synchronized

to the camera to illuminate the soil. Use of a strobe light source would 'freeze' the movement of the soil without having to stop the probe. The system would be designed for use with a cone penetrometer system thereby allowing real-time visualization of sub-surface sediment lithostratigraphy, texture, and possibly structure characteristics.

3.4 Task 3: Photogrammetric Algorithms for Grain Size Distributions

Quantifying particle size distributions and their moments is a fundamental part of characterization and modeling in the material sciences (Allen, 1997). In process engineering, for example, measurement and control of the particle size distributions can be used to control and predict the product and process characteristics. Within the last two decades, image-based particle size distribution (psd) estimation has emerged as a strong research direction to complement existing methods and to overcome some of their limitations. As a major observation, the progress in image-based psd research is strongly connected with two main factors. These factors can be summarized by the scientific development and advancement in several interrelated fields, such as digital image processing and computer vision, as well as the slow penetration of this scientific knowledge among different fields. These two factors are well reflected in the early and the recent techniques and algorithms for psd. For example, in the eighties and early nineties photo-sieving (Ibekken and Schleyer, 1986; Diepenbroek et al., 1992) was proposed as a method for image-based psd. Photo-sieving relies on manual identification and digitization of individual particle boundaries. On the other hand, Butler et al. (2001) utilized a simple global threshold approach for particles delineation or segmentation assuming that the image intensities follow a bimodal distribution. They tested an automated approach for threshold selection, but they found that it has a very poor performance and so the threshold was selected in a subjective way. It is clear that, in general, segmentation based on threshold alone will not produce acceptable results in the gamut of image segmentation applications.

Over the least five years or so, a gradual progression was made toward more sophisticated approaches for psd. For example, Ghalib and Hryciw (1999) presented a comprehensive approach for estimating soil psds using digital images acquired in a laboratory setting. They used a backlight illumination to enhance the contrast of the particles. Their approach started with a binary thresholding which was followed by distance transform and watershed segmentation for the final delineation of the particle regions. McEwan et al. (2000) used Canny edge detection followed by morphological dilation and skeletonization to delineate sediment particles imaged by a high-resolution laser altimeter. They argued that this approach could be extended to digital images with additional development. In another laboratory setting, Carter and Yan (2005) investigated the suitability of image-based particle size analyzer for measuring particle shape parameters, such as aspect ratio. They concluded that the imaging-based sensor is very capable of measuring the shape parameters within acceptable tolerance bounds.

Graham et al. (2005a) offered a detailed analysis of four approaches for automated particle size measurement of coarse-grained sediments that exceed 23 μm. All of the parameters that control the performance of these approaches were tested for every possible combination to identify the range of values that will give acceptable results. From a machine learning perspective, their testing methodology is equivalent to partial ensemble methods or classifier combinations (Tan et al., 2005). Graham et al. (2005b) developed a sophisticated image-based approach for psd that

followed as coarse-to-fine or a global-to-local strategy for particles or grain extraction. This approach starts with a non-linear smoothing by a median filter to remove the markings from the particle surfaces while preserving the edges. This step was followed by a morphological bottom-hat transform to identify small dark parts of an image. A double threshold approach was then applied to the transformed image to obtain an initial segmentation. The result was refined by a watershed segmentation augmented by minima suppression. The overall performance of the algorithm was optimized by a detailed assessment of its internal parameters and they are tuned to work with image particles that are greater than 23 μm. The final results required visual checking in case the segmentation step failed for some reason.

From the previous discussion, it is evident that the core of an image-based psd is highly dependable on a robust segmentation procedure to isolate the particle regions from their backgrounds. The success of any image segmentation algorithm is typically measured by the extent to which acceptable results can be achieved and the computational efficiency with which these results can be obtained. To this end, the objective of this task was to develop a general approach for image-based particle size distributions using an integrated and a multi-stage segmentation algorithm. The approach differs from that described by Graham et al. (2005b) in two major aspects: (1) it is very general and can be trained for any grain or particle size distribution; and (2) it addresses the complexity of the segmentation problem in an integrated and robust algorithm. This algorithm follows a gradual approach to come up with the hypotheses for the image regions that correspond to particles.

This new approach is collectively referred to as “Pixel-Vernier” or for short (PV). PV combines markers-controlled watershed segmentation, which will be explained in the next section, and a minimum-distance clustering thresholding algorithm for particle regions extraction. PV is following a gradual coarse-to-fine or local-to-global strategy to perform the extraction process. The current realization of PV works in a supervised mode that requires user training. This training is restricted to a single smoothing parameter to adapt PV to different material types. The extracted regions are used to derive several geometric attributes for each particle, such as the semi-major axis, the semi-minor axis, and the equivalent diameter. These geometric attributes of all particle regions are then used to estimate the particle size distribution and their relevant statistics. The PV can be used in a laboratory or field setting and for the purposes of this project was tested on a diverse set of materials including soils, rocks, Mars surface images, and digital images of varying texture.

3.4.1 Pixel VernierApproach

The Pixel-Vernier (PV) is a supervised approach for image-based particle size distribution (psd) estimation that uses a single training parameter. In addition, PV can also be viewed as a measurement approach for particles distribution estimation that exploits the human abstraction of decision-making at a very high level. The training parameter of PV is confined to the size of an averaging filter. The user checks the result visually at the training stage to determine if the results are acceptable or not in terms of delineating the optimal image regions that correspond to particles. The benefits of the averaging process can be appreciated from several angles such as minimizing the local random variability, increasing the probability of getting connected particle regions or removing markings on the particle surfaces, and introducing the bias of the PV user/s

toward a particular size distribution. From the classical setting of non-linear problems solving, the training step or the smoothing process can be perceived as the provision of the initial approximation for the segmentation algorithm to converge toward a particular size. This approximation does not have to be exact, but it has a wide radius of convergence. From this perspective, the zero approximation should be considered as one of the options. In other words, some applications may not require any approximations and the algorithm will converge to the correct size without smoothing. This is most likely to be the case for highly textured images such as fine grained soil.

After obtaining the optimal averaging window size by training, PV proceeds in two phases of segmentation to extract the particle regions following a coarse-to-fine strategy. At the coarse level, we developed markers-controlled watershed segmentation algorithm, which is also a two-stage process. In other words, the first stage is a collective action of preprocessing by markers and then followed in the second stage by the classical watershed segmentation. Markers are generally defined as local connected image regions that can be grouped based on homogeneity or other criteria of similarity (Gonzalez and Woods, 2002). The markers limit the number of image regions that will result from the watershed segmentation. At the fine level or the second stage, PV uses a minimum distance clustering algorithm for local segmentation within every region that results from the coarse level segmentation. The minimum distance clustering was developed to offset the remaining local over-segmentation that induced by the watershed algorithm. The final results of the of the minimum distance clustering, in terms of the final segmented image regions, is forwarded to a connected component labeling algorithm (Shapiro and Stockman, 2001) to identify and to extract each image region. Figure 1 shows the overall work flow of the Pixel-Vernier approach.

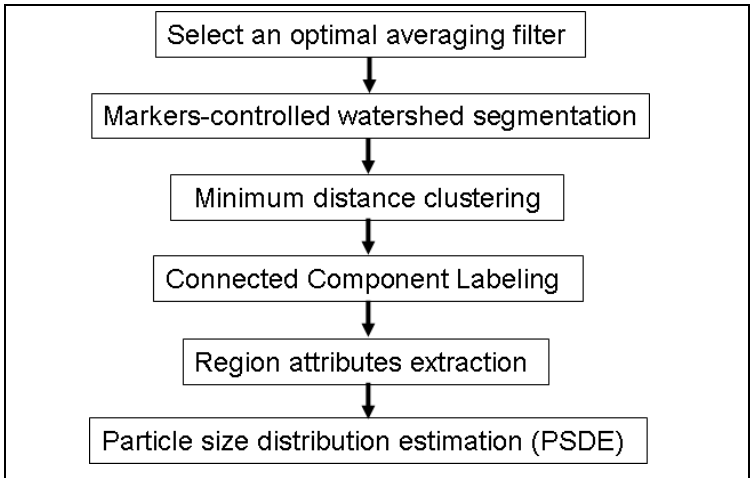

Figure 2. Overall work flow of Pixel-Vernier Approach

3.4.2 Markers-Controlled Watershed Segmentation Algorithm

The markers-controlled watershed segmentation is a powerful approach for image segmentation (Meyer and Beucher, 1990). This approach allows the development of practical solutions to the over-segmentation problem associated with the classical watershed algorithm by limiting the number of image regions. This limitation is typically achieved by adding a preprocessing step

(here: markers) that can bring extra knowledge into the watershed segmentation algorithm (Gonzalez and Woods, 2002). As a side remark, from a cognitive science perspective, markers can be viewed as a mechanism that brings a focus of attention to selected areas in the image. Itti and Koch (2001) defined attention as the process of selecting and gating visual information based on saliency in the image itself (bottom-up), and on prior knowledge about scenes, objects, and their interrelations (top-down). Practically, a marker is a local homogenous connected component (a region) that belongs to an image. By viewing the information content of an image as a foreground and a background, two types of markers could be defined: 1) an internal marker, and 2) an external marker, which belong to the foreground and the background respectively. Different types of image attributes can be used as markers such as intensity, color, edge gradients, texture, and even motion in the case of an image sequence. In general, a procedure for marker selection has two main steps: 1) the identification of the image attributes that will be used to define the marker; and 2) the implementation of the preprocessing.

In the context of the proposed approach, the marker control is achieved through the use of a set of ranking filters to enhance the information content of the image. The image intensities in a predefined local neighborhood are sorted according to their numerical values and then the central pixel in that neighborhood is replaced by a ranked intensity value selected according to a preset criterion such as the minimum or the maximum (Russ, 2002). In particular, the markers control step is applied as follows:

1. A circular local neighborhood, which has a radius of 5 pixels, is chosen for the ranked filters. The circular shape is chosen to minimize the directional effects of the local neighborhood.

2. Two new images are generated by convolving the original image by the maximum and the minimum rank filters. Let us call them the maximum image and the minimum image respectively. In fact, the maximum filter is nothing but the classical top hat filter (Bright and Steel, 1987).

3. Then, the maximum image is added to the original image to form a new image. The objective of this step is to enhance the local boundaries.

4. Then the minimum image obtained in step (2) is subtracted from the end result of step (3) to produce a new image.

5. A complement image is then computed for the new image obtained in step (4). To understand the notion of the complement image, we examine two examples. In the complement of a binary image, zeros become ones and ones become zeros. In other words, black and white are reversed. In the complement of intensity or gray level image, each pixel value is subtracted from the maximum pixel value (e.g., 255) supported by the class and the difference is used as the pixel value in the output image. In the output image, dark areas become lighter and light areas become darker.

6. The complement image is forwarded to the classical watershed segmentation algorithm to obtain the initial hypothesis for the particle regions.

3.4.3 Minimum Distance Clustering Algorithm

Although the combined approach of the markers-controlled and the smoothing process offer a solution to the global over-segmentation problem encountered in the watershed algorithm, it led to a local over-segmentation at a regional level. In other words, the image regions do not provide optimal information for the existing particles in terms of their spatial extent. To this end, we developed a minimum distance clustering algorithm to handle the local over-segmentation. The underlying principle of this algorithm is based on the assumption of separable intensity distribution within each image region into two classes, which is the classical objective of any binary thresholding approach. As a side remark, the result of binary thresholding depends on how the thresholding value or the decision-line is selected or obtained. For example, manual selection of the threshold reflects the human bias towards a particular intensity distribution. On the other hand, automatic selection of the threshold value typically reflects a certain statistical tendency. For example, Otsu's algorithm (1979) seeks the bimodal distribution between two classes by minimizing the within-group variance and maximizing the between-group variance. The minimum distance clustering algorithm is based on the following steps:

1. Searching for the minimum and maximum intensity values within each image region that resulted from the markers-controlled watershed segmentation.

2. Classifying the intensity values in each region into two classes according to their absolute distance from the minimum and the maximum intensity values in each particular region.

3. The pixels with intensity values that are closest to the maximum intensity are classified as particles and the ones that are closest to the minimum are classified as backgrounds. This classification assumes that the particle intensities have a bias toward the brightest or highest intensity values, but nothing wrong to take the opposite bias, which is application dependent.

Figure 3 shows a conceptual diagram for the minimum distance clustering algorithm. The oval on the top resembles a mixed intensity distribution, but after applying the minimum distance clustering algorithm is separated into two classed as shown by the left and right ovals on the bottom.

3.4.4 Geometric Attributes Extraction

Following Shapiro and Stockman (2001), the following region properties are derived from the results of the minimum distance clustering:

1. Region area, which is the number of pixels per each region.

2. Region boundaries.

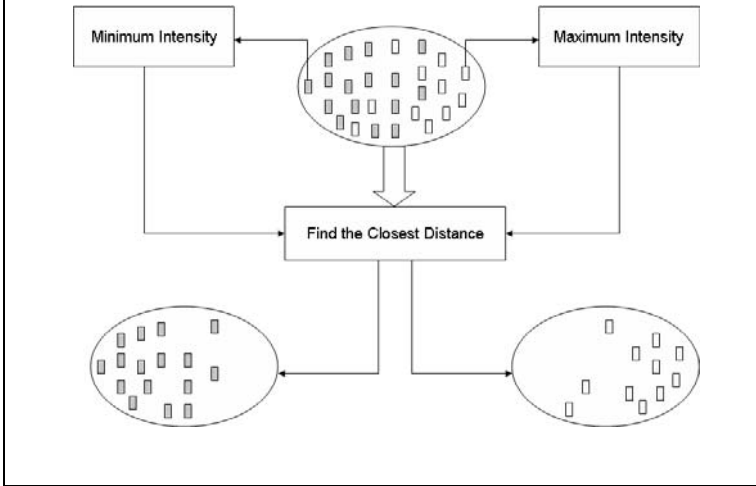

Figure 3. Conceptual diagram for the minimum distance clustering algorithm.

3. Perimeter length (P), which are the number of the pixels along the boundary of a region. The perimeter length is used to derive what is called the 'equivalent diameter (d_e)' as follows:

$$d_e = \frac{P}{\pi} \tag{23}$$

4. Region centroid, which combined with its boundary, is used to derive three types of moments. These moments are the second-order row moment, the second-order column moment, and the second-order mixed moments. These moments are combined to derive the geometrical attributes of the best fit ellipse to each image region. These attributes are the length of the major (*a*) and the minor (*b*) axes. Particle shape is the second most significant sediment property in natural sediments and can be defined by an anisotropy ratio, or by the shape factor. The average anisotropy of the extracted particles may be calculated as follows:

$$\text{Anisotropy} = 1 - \frac{1}{n}\sum_{i=1}^{n}\frac{b_i}{a_i} \tag{24}$$

For three dimensional measurements, all three axes can be determined and a shape factor, ψ, calculated as

$$\psi = \frac{c}{\sqrt{a\,b}} \tag{25}$$

where a, b, and c are the lengths of the major (longest) axis, the minor (intermediate) axis, and the semi-minor (shortest) axis, respectively. These axes are the mutually perpendicular axes of the particle. The shape factor for a sphere would be 1.0, whereas the shape factor of particles from natural sediment would be less than 1.0.

3.4.5 Particle Size Distribution and Statistics

The equivalent diameters, d_e, or diameters for short, of the entire collection of particles that exist within an image view are used to derive the cumulative distribution curve, which is obtained from a histogram. The information content (frequency counting) of each bin in the histogram is weighted by the corresponding areas of the diameters that contribute to each bin. This weighting is used to account for the actual 2-D coverage of the image regions or particles. Naïve frequency counting will lead to incorrect characterization of the particle size distribution curve. Mathematically, the frequency weighting of d_e is implemented as follows:

$$\hat{f}(d_e) = \sum_{i=1}^{m} A_i d_{e_i} \tag{26}$$

where $\hat{f}$ is the estimated frequency of d_e and A_i is the corresponding area for each d_e. Following Folk (1980), the cumulative distribution curve is used to estimate the following statistical measures:

a. Median, this is the d_e corresponding to the 50^{th} percentile on the cumulative curve,

$$\text{Median} = d_{e50\%} \tag{27}$$

b. Graphic mean (M_z) and is given by:

$$M_z = \frac{d_{16\%} + d_{50\%} + d_{84\%}}{3} \tag{28}$$

c. Inclusive graphic standard deviation, σ_I, is given by:

$$\sigma_I = \frac{d_{84\%} - d_{16\%}}{4} + \frac{d_{95\%} - d_{5\%}}{6.6} \tag{29}$$

d. Inclusive Graphic skewness (SK_I) averages the skewness obtained from $d_{16\%}$ and $d_{84\%}$ with the skewness obtained from $d_{5\%}$ and $d_{95\%}$ and is given by:

$$SK_I = \frac{d_{16\%} + d_{84\%} - 2 \times d_{50\%}}{2 \times (d_{84\%} - d_{16\%})} + \frac{d_{5\%} + d_{95\%} - 2 \times d_{50\%}}{2 \times (d_{95\%} - d_{5\%})} \tag{30}$$

SK_I determines the skewness of the central portion of the cumulative curve as well as the skewness of the "tails", and the tails are just where the most critical differences between samples lie.

e. Graphic kurtosis, and is given by:

$$K_G = \frac{d_{95\%} - d_{5\%}}{2.44 \times (d_{75\%} - d_{25\%})} \quad (31)$$

For normal curve, K_G=1.00; leptokurtic curves have K_G over 1.00; and platykurtic curves have K_G less than 1.00.

3.5 Particle Packing Characteristics

Both porosity and permeability are critical parameters for estimating water retention and hydraulic conductivity of heterogeneous subsurface formations. However, in situ measurements with direct push technology could be subject to error owing to rearrangement of pore space adjacent to the probe. Grain size distributions are less susceptible to the effects of probe insertion and can provide a robust estimate of porosity permeability using a packing model. Models have been developed to predict the porosity and permeability of binary mixtures but natural soils tend to be made up of numerous fractions. The objective of the subtask was to extend an existing packing model developed for binary packs of spherical particles to a multicomponent mixture of aspherical particles

3.5.1 Porosity of Binary Mixtures

Clark (1979) proposed an ideal packing model based on the assumption of complete mixing of two sizes of particles. This model recognizes two end-members, coarse-packed and fine-packed sediments. In coarse packing, the coarse grains form a self-supporting structure with a non-compacted porosity equal to ϕ_c. As the concentration of fines increase, ϕ decreases as the fines fill the pore space. This decrease continues until a critical point, c, where fines occupy all the pore space of the clean coarse-textured fraction. At this point, the fines concentration is equal to ϕ_c. Beyond this point, an increase in fines concentration is only possible by replacing coarse particles with fines. In this case, the coarse grains are increasingly dispersed in the matrix of fine grains. The porosity of the mixture, ϕ_b, is solely a function of the volume fraction of fine components. At the second end-member, the pack is composed of only fines without coarse particles and has a porosity of ϕ_f. The porosity of a binary mixture is calculated as:

$$\phi_b = \begin{cases} \phi_c - c(1-\phi_f) \; if \; c < \phi_c \\ \\ c\phi_c \qquad\qquad if \; c \geq \phi_c \end{cases} \quad (32)$$

In natural sediments, the mixing of two components is rarely complete and the ideal packing is difficult to achieve (McGeary, 1961). The ideal packing model was modified to account for fractional packing (Koltermann and Gorelick, 1995). The Koltermann-Gorelick (KG) model introduced a coefficient, y, to account for the relative proportions of coarse and fine materials in the mixture. The porosity of the mixture is then given as:

$$\phi_b = \begin{cases} \phi_c - cy(1-\phi_f) + (1-y)c\phi_f & if\ c < \phi_c \\ \phi_{\min} = \phi_c(1-y_{\min}) + \phi_c\phi_f & if\ c = \phi_c \\ \phi_c(1-y) + c\phi_f & if\ c > \phi_c \end{cases} \quad (33)$$

where ϕ is porosity; ϕ_c and ϕ_f are the porosities of the coarse and fine end-members, respectively, ϕ_{min} is the minimum value of ϕ; and c is the volume fraction of the fine fragment based on total volume. The value of y ranges from 0 to 1 with a maximum occurring when there is only one component (i.e., $c = 0$ or $c = 1$). A minimum in y, y_{min}, occurs when the pores of the coarse component are completely filled with fines, i.e., $c = \phi_c$. The value of y at volume fractions of fines is computed by linear interpolation:

$$y = \begin{cases} 1 - c\left(\dfrac{1-y_{min}}{\phi_c}\right) & if \quad c < \phi_c \\ y_{min} = 1 + \phi_f - \dfrac{\phi_{min}}{\phi_c} & if \quad c = \phi_c \\ 1 - (1-c)\left(\dfrac{1-y_{min}}{1-\phi_c}\right) & if \quad c > \phi_c \end{cases} \quad (34)$$

The KC model has been proven superior to the ideal packing model for predicting the porosities of binary mixtures. However, it is recognized that there are some limitations. First, the physical interpretation of parameter y is has not been demonstrated. Perhaps more importantly, for y_{min} $<(0.5 + 0.5\phi_f)$, the KG model predicts ϕ_{min} at a volume fraction of fines that is less than ϕ_c. This typically occurs when ϕ_{min} is relatively large, as is the case with coarser gravel fractions. Nevertheless, the KG model can be used to estimate the porosity of sediments when limited information on the grain-size distribution is available.

3.5.2 Saturated Hydraulic Conductivity of Binary Mixtures

One difficulty in applying the KC-type equations to estimate hydraulic conductivity of binary mixtures is the need to determine the representative grain diameter, d. A variety of approaches have been tried. Bear (1972) recommended using the harmonic mean. However, the type of averaging used to calculate d should depend on the type of packing because d is a function of the volume fraction of fine components (Koltermann and Gorelick, 1995). Once d is known, the saturated hydraulic conductivity of a binary sediment mixture, K_b, is given by

$$K_b = \left(\frac{\rho g}{\mu K_{cc} s_s^2}\right)\left[\frac{d^2\phi^3}{(1-\phi)^2}\right] \quad (35)$$

where ρ is fluid density, g is the gravitational constant, and μ is dynamic viscosity. The Kozeny-Carmen coefficient (Kozeny 1927), K_{cc}, is defined as the product of tortuosity (τ) and the shape factor (S_{hf}); both of which are dimensionless, i.e., ($K_{cc} = \tau S_{hf}$). The shape factor is a measure of the effect of the shape of the grains, pores, and pore channels in the porous medium. The tortuosity and shape factor reflect the geometry of the cross-sectional area of the pore channels normal to the flow direction. For unconsolidated sediments, Carman (1937) assigned a value of 2.0 for τ and a value of 2.5 for S_{hf} , which both results in a value of 5.0 for K_{cc}. Estimates of the shape factor can be derived from photogrammetric measurements.

Koltermann and Gorelick (1995) recommend that the geometric mean be used for mixtures with low concentrations of fines whereas the harmonic mean is recommended for mixtures with high concentrations. A recognized problem is that d is undefined for mixtures in which neither fraction is dominant. The result is a discontinuity in the $K(c)$ function (e.g., Fig. 8, Koltermann and Gorelick, 1995; Fig. 1c, Kamann et al., 2007).

Since K_b must be continuous across all d, including those where $0 < c < 1$, we introduce a power average as an aggregation operator over all c. A p-order power average (Korvin, 1982; Zhang et al., 2005) is defined as

$$d = [(1-c)d_c^p + c\,d_f^p]^{1/p} \tag{36}$$

where d_c and d_f are the mean diameters of the coarse and fine particles, respectively, and p is a coefficient that varies from positive to negative as the fine fraction increases. The arithmetic ($p = 1$), geometric ($p \rightarrow 0$), and harmonic ($p = -1$) are all specific cases of the power average and cover the entire range of mixtures.

3.5.3 Unsaturated Hydraulic Conductivity of Binary Mixtures

The challenge, therefore, is to use information on packing to derive constitutive properties for subsurface flow and transport. The water-retention function of the binary sedimentary mixture may also be described by the fractional packing model, i.e.,

$$\theta(\psi) = \theta_c(\psi) - c\left\{\left[\frac{\theta_c(\psi)}{\phi_c}\right] - \theta_f(\psi)\right\} \tag{37}$$

where θ is the volumetric water content, θ_c is the volumetric water content of the coarse fraction, θ_f is the volumetric water content of fine fraction, and ψ is the matric potential. It is well recognized that K_s increases with increasing mean particle diameter and the gravel concentration. However, a number of researchers have reported a threshold concentration above which K_s decreases, perhaps owing to less accessible surfaces for water flow (Valentin and Casenave, 1992; Valentin, 1994). Such a threshold is consistent with the concept of the critical ratio of entrance and the porosity minimum. Hence, a similar approach can be used to estimate the unsaturated hydraulic conductivity, $K(\theta)$, i.e.,

$$K(\theta) = K_c(\theta_c)\left[1 - \left(\frac{c}{\phi_c}\right)\right]^b + c\,K_f(\theta_f) \qquad (38)$$

In Eq. (38) K_c and K_f are the hydraulic conductivities of the coarse-grained and fine-grained components, respectively, whereas b is a fitting parameter. Equations 37 and 38 may then be used to estimate the unsaturated hydraulic properties of binary mixtures based on the properties measured on the end members. However, these equations are not readily applicable to the multicomponent mixtures typical of natural soils.

3.5.4 Porosity of Multicomponent Mixtures

Natural soils typically contain multiple components that show significant differences in particle shape, density, and porosities among size fractions. A heterogeneous soil can be treated as an assemblage of n fractions of aspherical particles (Yu et al., 1996a,b). Each fraction, i (i =1, 2, ..., n) has an equivalent volume diameter, d_{v_i} ; sphericity, φ_i; volume fraction, X_i; and mean particle density, ρ_i. The type of packing arrangement is reflected in the specific volume of particles, V_s. The specific volume, V, of the multi-component pack may be expressed as (Yu and Standish, 1993)

$$V = f(V_s, X_1, X_2, 5\ \ , X_n; d_{v_1}, d_{v_2}, 5\ \ , d_{v_n}; \varphi_1, \varphi_2, 5\ \ \varphi_n) \qquad (39)$$

The mixing interaction between two components is dependent on their relative size, which may be quantified using an equivalent packing diameter (Yu and Standish, 1993). The equivalent packing diameter of a size fraction can be determined by measuring its size-dependent packing properties and relating them to the diameter of a sphere as a result of the similarity between spherical and aspherical particle packs. Component i should therefore have an equivalent packing diameter d_{p_i} that is a function of d_{v_i} and φ_i. The porosity, ϕ_b, of a multicomponent mixture may then be calculated as (Yu and Standish, 1993; Yu et al., 1996a,b),

$$\phi_b = f(X_1, X_2, 5\ \ , X_n; d_{p_1}, d_{p_2}, 5\ \ , d_{p_n}; \phi_1, \phi_2, 5\ \ \phi_n) \qquad (40)$$

where X_i is the fractional solid volume of the i^{th} component.

The specific volume of the multicomponent mixture, V, defined as the reciprocal of the packing density, is calculated as the maximum of V_i^T :

$$V = \max\left\{V_1^T, V_2^T, 5\ \ , V_n^T\right\} \qquad (41)$$

where

$$V_i^T = \sum_{j=1}^{i-1}\left[V_j - (V_j - 1)g(r_{ij})\right]x_j + V_i x_i + \sum_{j=i+1}^{n} V_j\left[1 - f(r_{ij})\right]x_j \qquad (42)$$

In Eq. (42), V_i is the initial specific volume that can be determined from measurements of the initial porosity of each fraction, ϕ_i. The variable r_{ij} is the ratio of small-to-large equivalent packing diameters between components i and j. The two functions $f(r_{ij})$ and $g(r_{ij})$ are interaction

functions that depend on r_{ij}. Yu et al. (1996a,b) showed that for spherical particles, $f(r_{ij})$ is given by

$$f(r_{ij}) = (1 - r_{ij})^{3.33} + 2.81 r_{ij} (1 - r_{ij})^{2.77} \quad (43)$$

whereas $g(r_{ij})$ is given by

$$g(r_{ij}) = (1 - r_{ij})^{1.97} + 0.36 r_{ij} (1 - r_{ij})^{3.67} \quad (44)$$

The solution of Eqs. (39 to 44) requires prior information on ϕ_i and d_{p_i}. Both of these variables may be determined from measurements on the separated soil fractions.

In the absence of empirical data, it has been established that the ϕ_i of the spherical particles ranges from 0.4 for loose or poured packs to 0.36 for dense random packs (German, 1989). However, fine particles are typically aspherical, and ϕ_i increases as particle size decreases (Wakeman 1975; Yu et al., 1996a,b). Therefore, unlike the packing of coarse particles, ϕ_i is a function of particle size and shape. By representing the particle size and shape of component *i* with an equivalent volume diameter, d_{v_i}, and shape factor, ψ_i, ϕ_i may be calculated as

$$\phi_i = f(d_{v_i}, \psi_i) \quad (45)$$

To account for the aggregation phenomenon in the finer components, an equivalent packing size, d_{p_i}, that depends on both d_{v_i} and ψ_i, is defined as

$$d_{p_i} = f(d_{v_i}, \psi_i) \quad (46)$$

Yu et al. (1996a,b) have established dependencies between ϕ_i and ψ_i and between d_{p_i} and ψ_i for spherical particles. However, these relationships do not hold for fine particles because these particles are typically aspherical, and the interaction between particle size, shape, and porosity is not well understood. Nonetheless, the initial porosity can be easily measured for different components and related to d_{v_i}, in which case, Equation (46) reduces to

$$\phi_i = f(d_{v_i}) \quad (47)$$

For simplicity, it is assumed that the ratio of packing sizes between components *i* and *j*, r_{ij}, is dependent on the corresponding ratio of equivalent volume diameters, R_{ij}, i.e.,

$$r_{ij} = f(R_{ij}) \quad (48)$$

For a given fraction, Equations 47 and 48 can be developed empirically. However, other measureable parameters like particle diameter can be used in place of the equivalent volume diameter. Different types of fine particles (e.g., clays such as montmorillonite, illite, or kaolinite) are also likely to have different cohesive and packing behaviors, but these differences are ignored at this stage. Input parameters for the model therefore includes, for each size fraction, the shape factor, mean particle density, and porosity. Measurements were conducted on soil separates to determine these parameters. Initial porosities were determined for the different size fractions separated by wet sieving and sedimentation.

3.5.5 Porosity Measurements

For tests on binary mixtures, materials from two different size categories (paired from among three categories: silt, sand, and marbles/pebbles) were used to create binary mixtures as simple models of gravelly sediments. The mixtures were created using glass sandblasting beads ranging in size from 2 to 14 mm (Potters Industry, Brownwood, TX) and glass marbles (14 mm, 50 mm) to represent the different subclasses of gravel, and commercially available 20/30 Accusand (Unimin Corp., LeSueur, MN) to represent the fine fraction. The glass beads were obtained as presorted fine, medium, and coarse fractions and were resorted, via sieving, before use. Additional binary mixtures were created using silt and fine gravel (4 mm) from the Hanford Site. For the experiments, samples were created with each end-member category (i.e., 100% fine, 100% coarse) and with mixtures of fine and coarse fractions. For each mixture, 10 samples were created by increasing the fines content from 0% to 100% in 10% increments. These samples were used in a series of experiments to measure physical and hydraulic properties.

Packing of the model mixtures involved used three approaches: 1) poured packing, 2) tapped packing, and 3) vibrated packing. For the poured pack measurement, a sediment sample was slowly poured into a standard laboratory funnel with a 5 mm opening, allowing the sediment to fill a graduated cylindrical (60 mm high, 50 mm diameter). The excess soil was levelled off and a rubber stopper that fit the opening in the cylinder was then placed on the surface. The stopper was fitted with two small holes (1 mm diameter) to allow any trapped air to escape. Placement of the stopper typically resulted in a small decrease in height and a leveling of the surface. The final height was used to calculate the poured packing density, ρ_0. After this measurement, the cylinder was subjected to manual vertical tapping until there was no change in the soil height. The tapping number and the height of the powder in the cylinder were recorded and used to calculate the tapped density, ρ_t. Finally, the cylinder was vibrated on a laboratory orbital vibrator and the final soil height recorded for use in calculating the vibrated density, ρ_v. Since the volume-height relation had been accurately calibrated, the measured height and weight of the soil in the graduated cylinder could be used to calculate the packing density. The measurements were repeated to quantify the end-member porosities of soil fractions separated on 1ϕ (2mm) intervals.

3.5.6 Hydraulic-Conductivity Measurements

To quantify the effect of grain size on hydraulic conductivity, the saturated hydraulic conductivity of end-member fractions and binary mixtures were measured in specially constructed permeameters. The permeameters were designed such that the specimen cylinders were approximately 8 or 12 times the maximum particle size of the sediment to be characterized (*ASTM* 2006). To measure K_s, enough sediment was first weighed out to pack the permeameter to a height of 15 cm at the desired density. The material was placed into the permeameter using a long tube to avoid segregation during emplacement. The tube was moved in a circular pattern and was maintained at a height such that the free fall of the sediment was not more than 3 cm. The permeameter was then vibrated to obtain the required packing density. The system was connected to a water supply, and water was allowed to flow upward through the sample at the desired rate until the flow became steady. The volume of water, Q, passing through the cross-sectional area, A, of the permeameter was recorded as a function of time, t. The hydraulic-head gradient ($i=\Delta h/L$) was also determined from the piezometers installed at the top and bottom

(separated by distance L) of the permeameter. Measurements were repeated using the size fractions, binary mixtures, and the end members of the binary mixtures at several flow rates. For each sample, the hydraulic-head gradient was plotted against the Darcy velocity (v=Q/A), and the K_s was determined from the slope of the line.

4. Results

4.1 Borehole Permeameter

4.1.1 Numerical Experiments

To test the theory, we conducted numerical simulations of water movement from a prototype borehole permeameter into a surrounding soil using the STOMP numerical simulator. A cylindrical coordinate system was used. The simulation domain size was 100 cm×10°×235 cm and was discretized into 44×1×94 nodes. Four soils with different textures, i.e., sand, sandy loam, silty loam, and clay loam, were used. The true hydraulic properties of the four soils were selected from Carsel and Parrish (1988) and were summarized in Table 1. For each soil, 10 measurements were were simulated at the tensions ranging from 0.05 m to 0.8 m.

Table 1. Soils and their hydraulic properties used in the numerical experiments (after Carsel and Parrish, 1988).

Soils	θ_s ($m^3\ m^{-3}$)	K_s ($m\ s^{-1}$)	α (m^{-1})	n (-)	θ_r ($m^3\ m^{-3}$)
Sand	0.43	8.25×10^{-5}	14.5	2.68	0.045
Sandy Loam	0.41	1.228×10^{-5}	7.5	1.89	0.065
Silty Loam	0.45	1.25×10^{-6}	2.0	1.41	0.067
Clay Loam	0.41	7.22×10^{-7}	1.9	1.31	0.095

To estimate the hydraulic conductivity, the Brooks and Corey (1964) model and the Gardner (1958) models were used. Figure 4 shows the linear relationship between *ln(Q)* and *ln(h)* and comparison of measured hydraulic conductivity (points) and their true values (solid line) for the sand using method 1, which uses the Brooks and Corey (1964) model. Corresponding results are shown in Figure 5 for the sandy loam, the silty loam Figure 6; and the clay loam and in Figure 7. These results show that, for the two coarse soils (Figure 4 and Figure 5) the measured values match the true curve very well, although the unsaturated hydraulic conductivity varied by 4 to 6 orders of magnitude. These results indicate that the proposed method 1, based on the Brooks and Corey (1964) model should work well for relatively coarse soils.

Results for sols with finer texture show an increase in the estimation error. The increase in the error is due to the large difference between the van Genuchten (1980) model and the Brooks and Corey (1964) model. For the two finer soils, the results were analyzed using method 2 and method 3, which uses the piece-wise linear hydraulic function based on the Brooks and Corey (1964) model and Gardner (1958) model. These results are shown in Figure 6 through 8. Both methods resulted in a significant reduction in the measurement error, whereas method 3 slightly underestimated K for the two soils. A significant difference between methods 2 and 3 is that the former uses the ln(Q) vs. ln(h) relationship while the latter uses the ln(Q) vs. h relationship. Hence, for measurements taken at water contents near saturation ($h \rightarrow 0$), method 2 may not be the most appropriate but method 3 can be used.

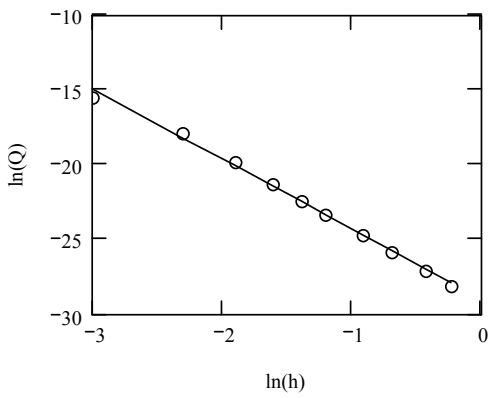

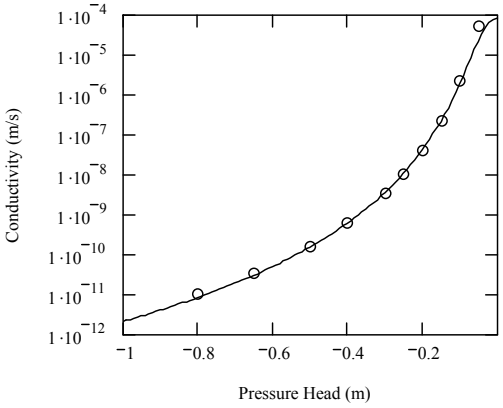

Figure 4. (a) Linear relationship between ln(Q) and ln(h) and (b) comparison of measured hydraulic conductivity (points) and their true values (solid line) for the sand using method 1.

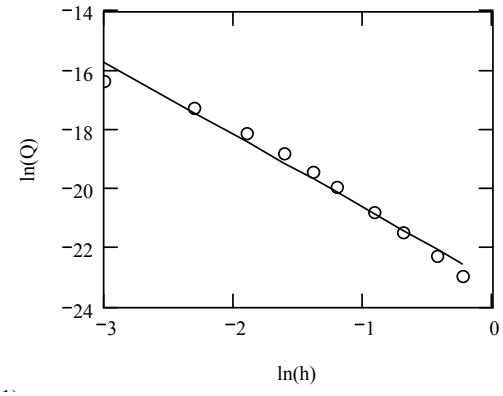

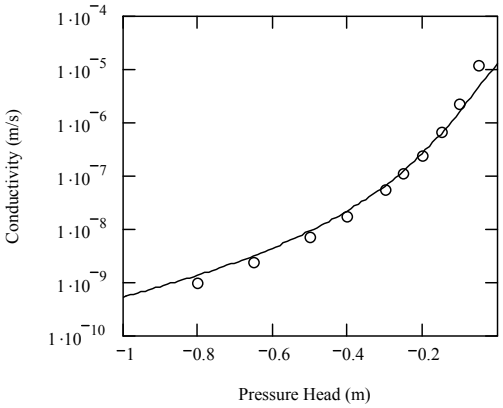

Figure 5. (a) Linear relationship between ln(Q) and ln(h) and (b) comparison of measured hydraulic conductivity (points) and their true values (solid line) for the sandy loam using method 1.

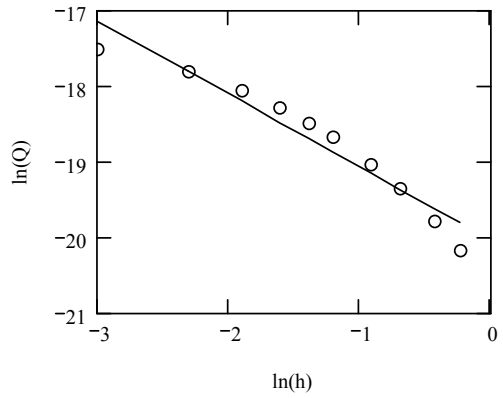

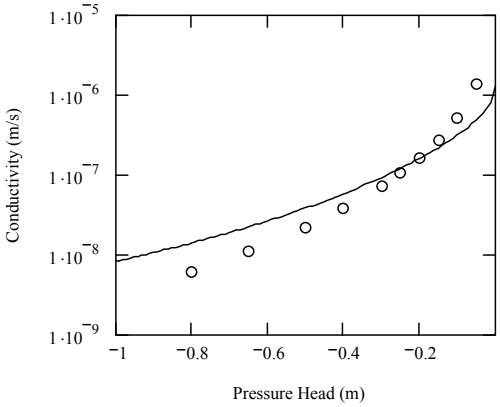

Figure 6. (a) Linear relationship between ln(Q) and ln(h) and (b) comparison of measured hydraulic conductivity (points) and their true values (solid line) for the silty loam using method 1.

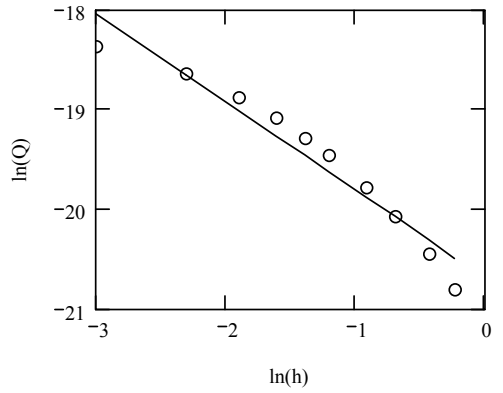

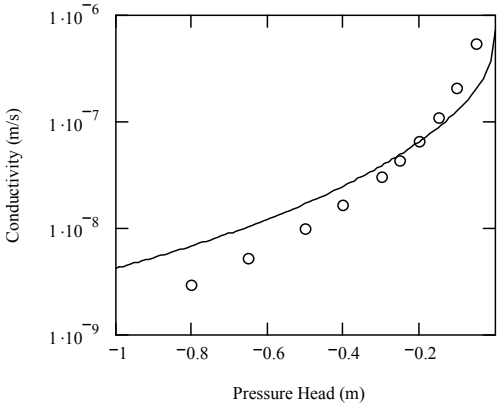

Figure 7. (a) Linear relationship between ln(Q) and ln(h) and (b) comparison of measured hydraulic conductivity (points) and their true values (solid line) for the clay loam using method 1.

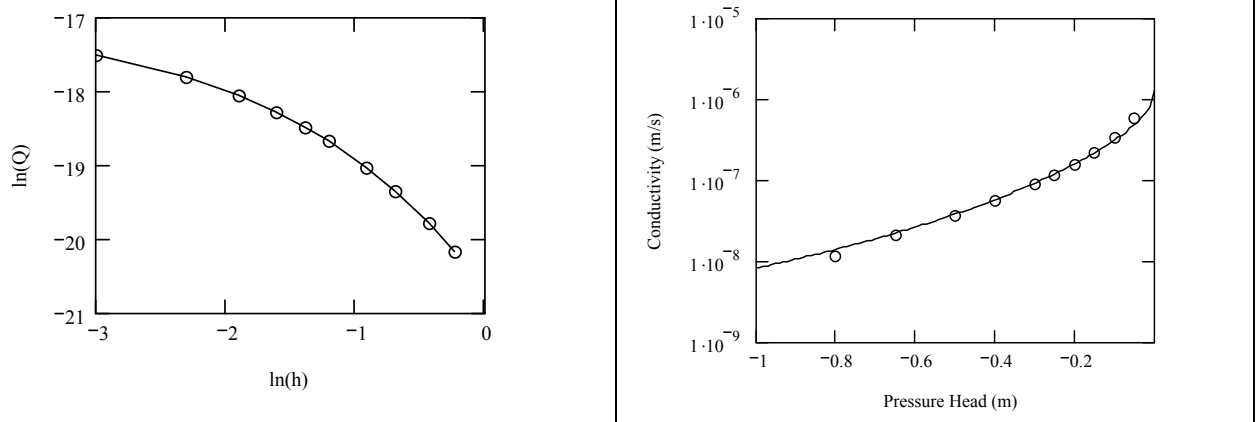

Figure 8. (a) Piece-wise linear relationship between ln(Q) and ln(h) and (b) comparison of measured hydraulic conductivity (points) and their true values (solid line) for the silty loam using method 2.

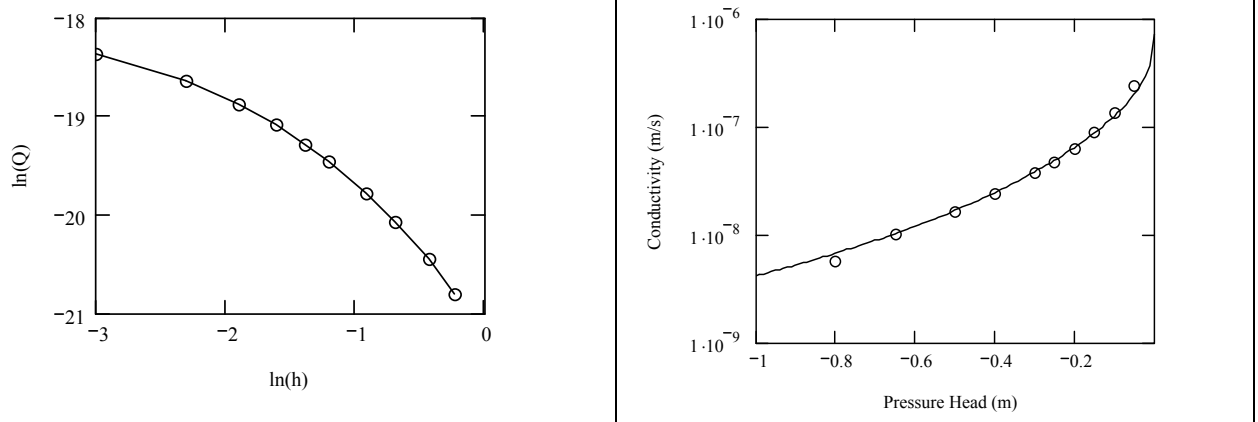

Figure 9. (a) Piece-wise linear relationship between ln(Q) and ln(h) and (b) comparison of measured hydraulic conductivity (points) and their true values (solid line) for the clay loam using method 2.

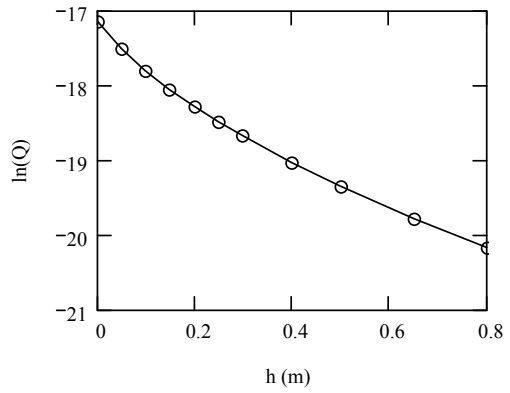

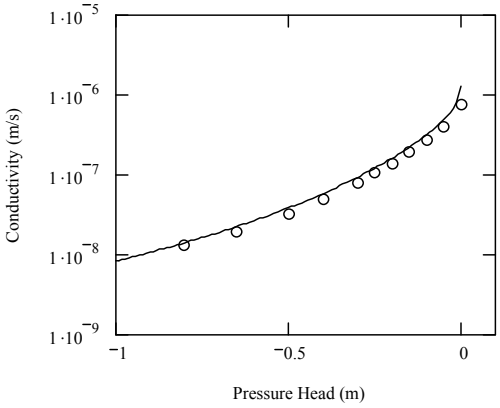

Figure 10. (a) Piece-wise linear relationship between ln(Q) and ln(h) and (b) comparison of measured hydraulic conductivity (points) and their true values (solid line) for the silty loam using method 3.

Although method 1 may give larger error in the finer soils, it may still be a more desirable approach as it is relatively easy to extrapolate the log linear slope to larger tensions whereas the slopes from methods 2 and 3 cannot be easily extrapolated due to piece-wise linear nature. Of-course, this problem can be overcome through use of a polynomial function to describe the piece-wise linear relationship. Nonetheless, the results if the numerical simulations show that a borehole tension permeameter would allow reasonable estimates of the hydraulic conductivity based on in situ measurements.

4.1.2 Laboratory and Field Experiments

A number of prototype borehole tension permeameter were constructed for testing in the laboratory and field. Early designs used a flexible porous material and porous plastic, with later designs based on porous stainless steel. To measure of the unsaturated hydraulic conductivity, K(h), the permeameter was connected to a Marriott system to control the tension, and the flow rate, Q(t) measured over time. The measurements were taken from large tension (relatively dry) conditions to small tension (relative wet) conditions. Measurements were taken both in the laboratory using grab soil samples and *in situ* for the field tests. Results were compared with those using other methods such as the Guelph Permeameter, instantaneous profile and constant flux methods and the inverse method (Zhang et al., 2003).

The unsaturated hydraulic conductivity of Hanford's BWTF sand was measured using the prototype Borehole Tension Permeameter both in the laboratory using grab samples and in the field. Soils used in the test were mostly sand so only method 1 was used to analyze the data. The results are shown by the points in Figure 11. For the purpose of comparison, the *K(h)* curves measured using other methods, i.e., the Guelph Permeameter, instantaneous profile and constant flux methods and the inverse method given in Zhang et al. (2003), are also shown. As expected, the *in situ* measured *K(h)* values were smaller than those measured in the laboratory by more

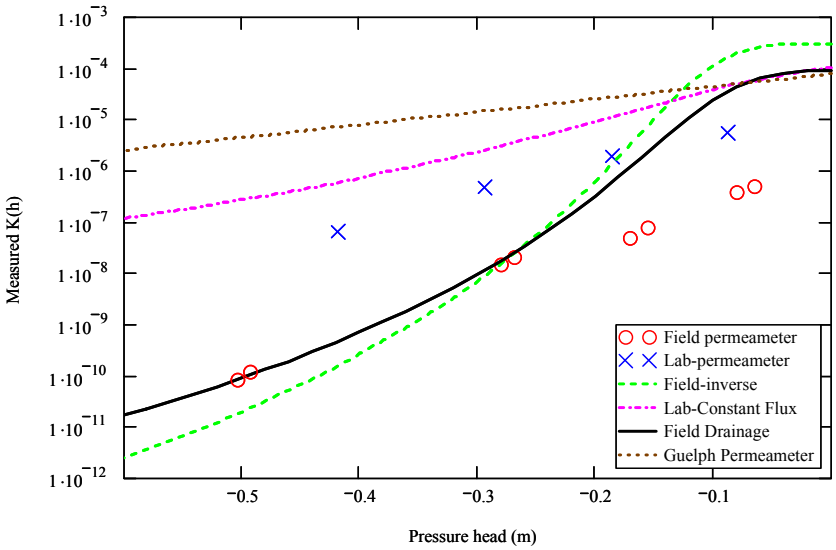

Figure 11. Comparison of the unsaturated hydraulic conductivity of Hanford's BWTF sand measured using the borehole tension permeameter and other standard methods.

than one order of magnitude. The *K(h)* curve based on the prototype permeameter results is nearly parallel to the curve derived from the constant flux method. For field measurements, at a tension of 0.3 m, results from the prototype permeameter were nearly identical to those from the instantaneous profile method and the inverse method, while those at smaller tensions (about 0.18 and 0.08 m) were smaller than the values from the latter two methods. One possible explanation for the smaller *K* values under relative wet conditions is that water from the permeameter is not entering the larger pores at the tensions used whereas the field instantaneous profile and inverse methods were based on an internal drainage and redistribution from saturated conditions and were dominated by larger pores at early times.

Under these conditions it would have been difficult to retain a positive heads in the cavity to measure hydraulic conductivity using traditional borehole methods. These results clearly show that the borehole tension permeameter is capable of providing reasonable estimates of the unsaturated hydraulic conductivity. Measurements near saturated conditions could be constrained by estimates from the Kozeny-Carmen equation taking into account the shape factor and grain size moments derived from photogrammetric measurements with the dual camera microscope system. The final design of the dual camera microscope is summarized below.

4.2 Dual-camera Microscope Imaging System

The original GeoVis probe was designed for use with the Elmo MN400 camera therefore the hardware was first modified to accommodate the final camera. First as a new optics fixture had to be designed to accommodate the new optics and to fix a glare problem noted with the original design. Evaluation of the lenses has resulted in the Edmund Optics Infinistix NT54-677 being rated as having the best image quality. The Infinistix lens is available in a range of magnifications and working distances. For the narrow FOV camera (FOV will be 1.5 mm to 2 mm) the Infinistix NT55-355 with optional doubler was acquired. One Infinistix lens (NT54-677) had a magnificaton of 1:1, and the second lens had a magnification of 2:1 and with an Infinity DL doubler that increases the magnification to 4:1. The new module included the following optical components: 1) an Infinistix 1.0X video lens with a 68-mm working distance (PN NT55-357); 2) an Infinistix 2.0X video lens with a 44-mm working distance (PN NT55-355); 3) an infinity DL doubler tube for the vide lenses, (PN NT39-686); 4) a 10-mm rhomboid prism (PN NT47-213); 5) a 10-mm right angle mirror (PN NT45-592); and 6) a 10-mm cube beamsplitter (PN NT32-601). All of the components were sourced from Edmund Optics. After evaluating a number of video cameras, the Sony XC-555 video camera was selected and two were installed so that there are matching cameras used for both the wide and narrow field of view systems. The Sony camera proved to be more flexible in that the automatic gain can be disabled, which allows for more consistent quantification of soil color and brightness.

A number of methods were investigated for simultaneously capturing data from the two video cameras. One method was to use a video combiner, which combined the two video streams into one video stream. While this would naturally provide timing synchronization between the two videos, a major disadvantage would be a significant reduction in image resolution. The two videos would have to share the standard video resolution of 720 pixels by 480 pixels, so the effective image resolution would be less than half of what the cameras can produce. Owing to the high data rate for video recording, a single computer proved to be insufficient to handle both video streams simultaneously. Ultimately, a second computer was installed into the monitoring system to record the video stream from the second video camera. That is, the narrow and wide field of view cameras needed their own video capture/recording system. A closed caption encoder was also incorporated to allow text data (such as push depth and time) to be embedded into the video stream on the vertical blanking line used for closed captions. This method of adding text data to the video stream has the advantage of giving the end user the option of displaying the data or not. Although it is best that video images captured for photogrammetric analysis are collected without the text being part of the captured image, it is very useful to have key information (such as the time and depth of the push) tied to the video stream. The closed caption system provides both in that the user can choose to display (or not) the text data. Closed caption display is available on any television manufactured in the past decade.

Figure 12 shows schematics of the modified probe. This design provides a 12 degree included angle between the two cameras. The narrow field of view lens is the Infinistix video lens with a 44-mm working distance and a magnification of 2X used with a 2X doubler tube, for a total magnification of 4X and a field of view of 1.6 mm. The wide field of view lens is the Infinistix video lens with a 68-mm working distance and a magnification of 1X and a field of view of 6.4 mm. Images takes with the 6.4-mm field of view represent the upper range of grain sizes that can be captured. Images from with the 1.7-mm field of view represent the current lower limit of resolution and correspond to the upper boundary for the silt-sized fraction. The capture hardware used for the

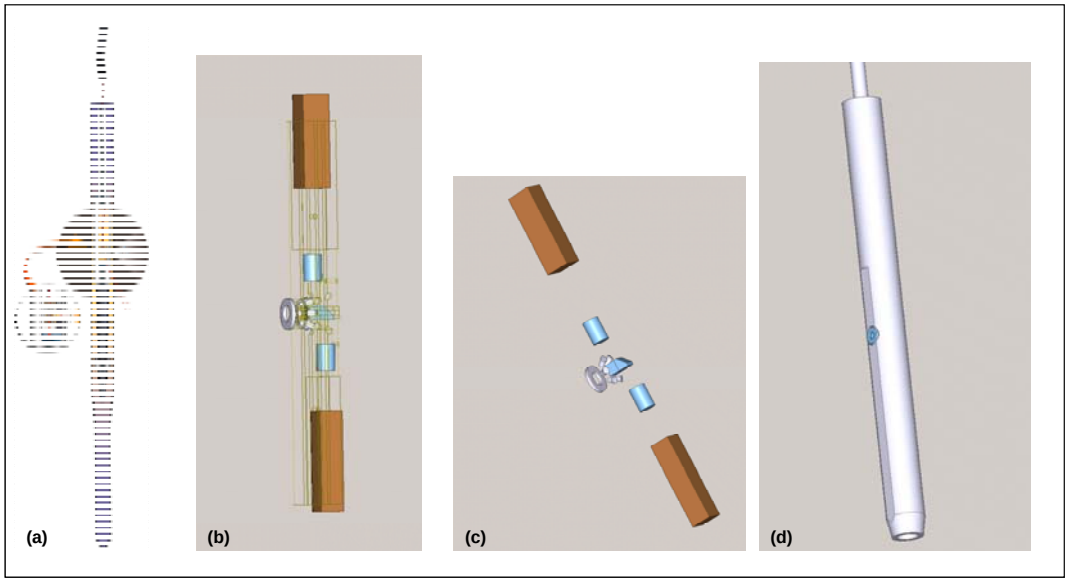

Figure 12. Schematic of original and modified GeoVis system, (a) original single camera soil imaging video microscope system, (b) internal view of dual-microscope system, (c) optical components including two cameras, lenses, beam splitter, prism and sapphire window, and (d) external view of new probe.

video microscope images is a Plextor ConvertX PX-M402U, an external USB 2.0 video capture device. The required dual optical path was accomplished using a 10×10×10 mm cubic beam splitter and a right angle prism. The lighting is provided by an array of 6 white light emitting diodes (LEDs). The components of the camera system are summarized in Table 2.

Table 2. Component specifications of the dual camera system

Component	Specification
Camera	Sony XC-555 All-in-one Industrial Micro Camera
Image Device	½" type CCD
Effective Picture Elements	768 (H) x 494 (V)
Video Output	S-video or Composite Video
Light Source	6 LED's, 5mm diameter White, clear lens, Intensity: 8000 mcd @20mA
Current Push Depth	up to 30 meters

A cutaway view of the stereo vision camera system with one camera is shown in Figure 13. This design includes a 12 degree angle between the two cameras. The modified probe also required a new umbilical be designed to handle the video signal. The video signal must travel through greater than 150 feet of umbilical to reach the video capture devices in the SCAPS truck. Previously, only a single camera was used and the output was composite video. A single coaxial cable of 0.10 inch diameter was used. The digital recording standard used for that system was MPEG1 with a resolution of 352 by 240 pixels.

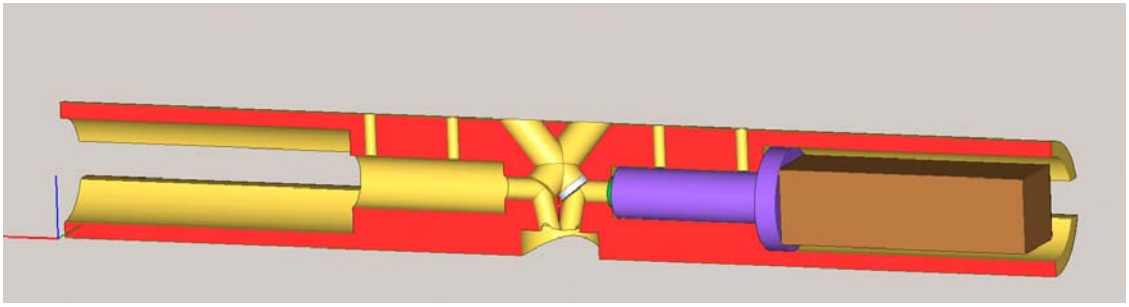

Figure 13. A cutaway view of the dual-camera stereo vision system with one camera/lens visible.

For the dual-video microscope system, the digital recording standard was MPEG2 with a resolution of 720 by 480 pixels, producing 4 times the resolution of the MPEG1. Owing to the higher resolution, a decision also had to be made about the recording system. The Sony XC-555 cameras can output either s-video or composite video. The s-video output sends out the color and brightness information on separate channels which produces a higher quality image than is possible with composite video, but at the cost of requiring two video signal cables per camera. The main constraint is the inner diameter of the push rods used in the SCAPS system. The video cable(s), power cable, and strain gauge cable for the tip and sleeve, with protective jacket, must all fit inside a 0.63" inner diameter.

Various types of cabling were evaluated for their suitability for this task. One option for transmission of the video signal was a CAT-5 Ethernet cable. Several companies make small video to CAT-5 adapters, which claim to be able to send video 100's of feet through CAT-5 cable. A single CAT-5 cable with 4 twisted pairs would be able to carry the S-video signal from both cameras but the effect on image quality was unknown. The CAT-5 cabling solution was to use commercial video to CAT-5 adapters so as to use CAT-5 cable for the long (>200 feet) cable runs. A single CAT-5 cable could carry the s-video signal from both cameras. Another possible solution is to use small diameter (~0.10" o.d.) 75 Ω co-axial cable. Two coaxial cables for each s-video signal were required, resulting in a total of four coaxial cables for the two cameras. Both cables were built to evaluate effects on long cables on image quality.

The effect on the image quality was evaluated by capturing images of the same object using the different cables for linking to the capture device. Figure 14 shows the results of these measurements. One object imaged was the cover for a software manual. This was chosen because of the color

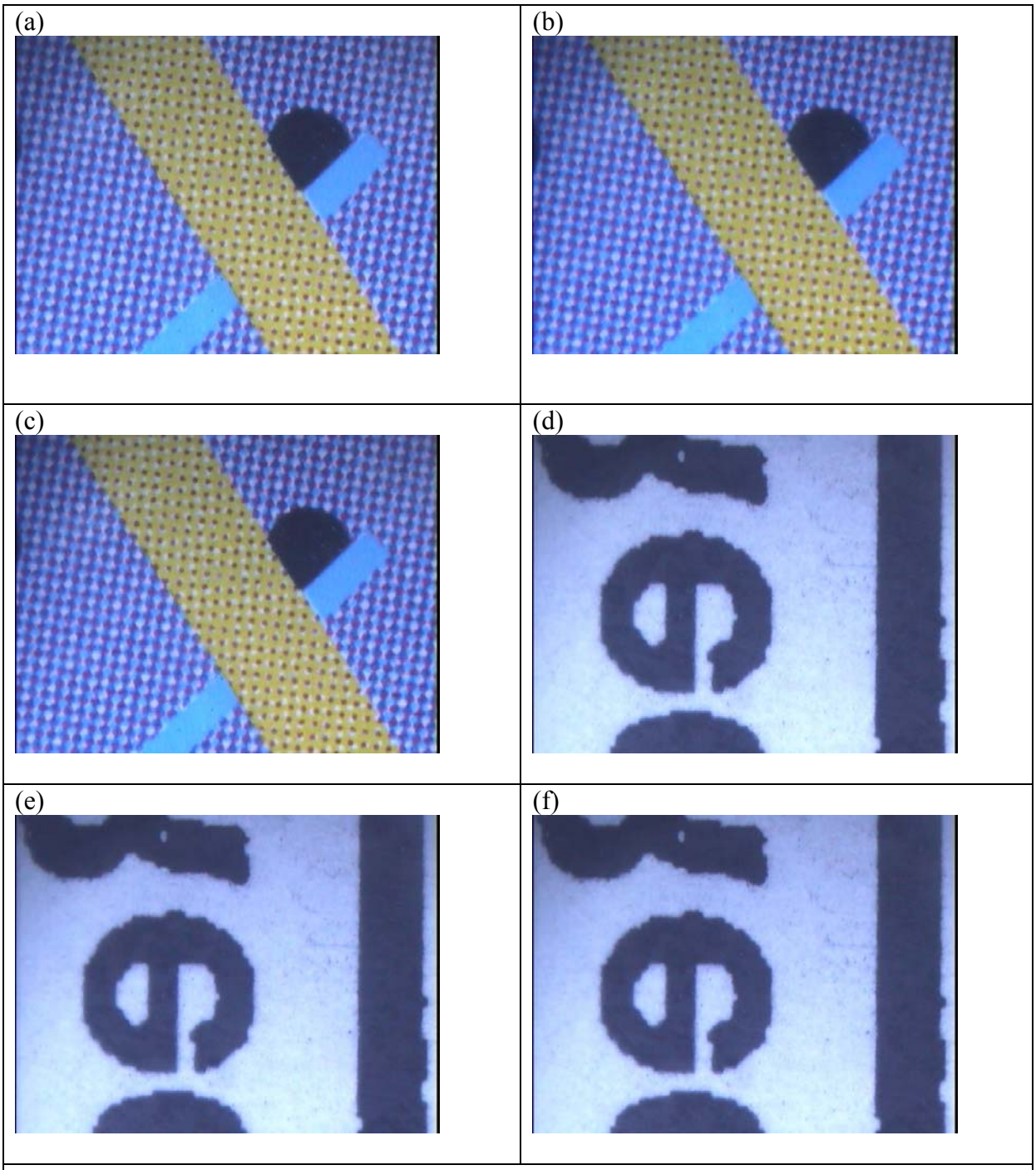

Figure 14**.** Digital images of objects used to test the effects of cable type and length on image quality, (a) manual cover at FOV of 6.4 mm with direct video connection using a 6-foot s-video cable, (b) manual cover at FOV of 6.4 mm with 200-foot CAT-5 video connection, (c) manual cover at FOV of 6.4 mm with 200-foot coax video connection (RG-179B), and (d) printed material at FOV of 6.4 mm with direct video connection (6-foot s-video cable), (e) Material at FOV of 6.4mm with 200-foot CAT-5 Video Connection and (f) printed material at FOV of 6.4 mm with 200-foot coax video connection (RG-179B).

content. The other object used for the image was black text printed on a sheet of paper. This was considered useful for the evaluation of the sharpness of the images. There are three images shown of each of the two objects. For reference, the first image was captured using a direct link to the capture card. The direct link used a 6-foot length of high quality s-video cable. Then an image was captured using a 200-foot CAT-5 cable with video adaptors (MuxLab™ Model 500016) at each end. The third image of each object was captured using the two coaxial cables (RG-179B). All images were captured using the wide field of camera (6.4-mm FOV). For reference this consists of a Sony™ XC-555 color video camera and an Infinistix lens of 68 mm focal length and 1X magnification. The Pinnacle Studios PCI 700 video capture card was used for the image capture. Visual inspection of the images shows no obvious degradation or flaws in the images due to the long cables. Given these results, the choice between the two cable systems depended on which was most robust, the easiest to assemble, and the one that minimized interference between the two camera systems.

Photographs of the new optics module are shown in Figure 15 and Figure 16. These images show views of the back side with the camera and front side with the sapphire window. Several test images of different materials were taken with the dual-camera microscope. These images were taken with the 6.4 mm field of view (FOV) and represent the upper range of grain sizes that can be captured and the 1.7-mm FOV, which represents the current lower limit of resolution with corresponds to the upper boundary for the silt-sized fraction. Figure 17 shows example images captured with the new dual camera system with the sapphire window in place. The camera was used to photograph black 120 grit sand paper with narrow and wide fields of view to evaluate adequacy of lighting and the effects on resolution. This very dark material presents the worst case for the lighting.

(a)

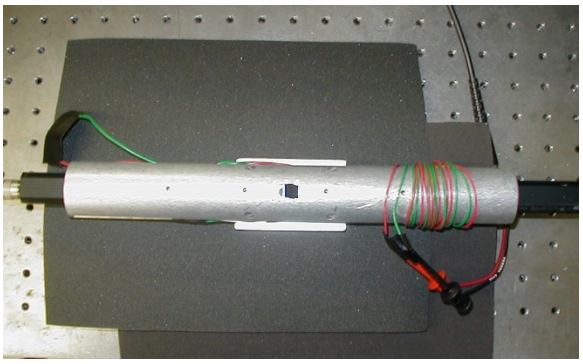

(b)

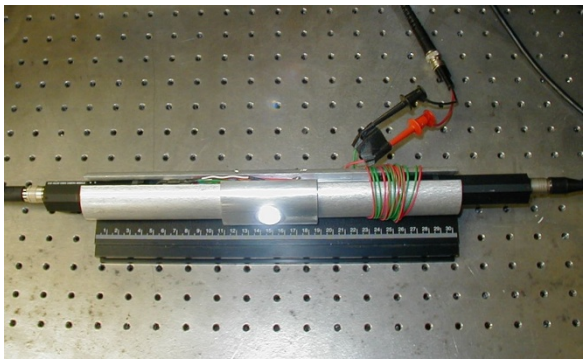

Figure 15**.** New dual camera module showing (a) view of back side, and (b) view of sapphire window side with LEDs turned on.

Laboratory tests of the prototype dual camera imaging system revealed a glare problem with the wide field-of-view (FOV) camera (FOV of 6 mm to 10 mm). The light from the LEDs was reflected from the inside surface of the sapphire window into the FOV of the camera. This was particularly problematic at FOV's greater than 6 mm. As a result of this the hardware was modified to increase the angle of incidence of the LED light and the window from the current 30 degrees to 45 degrees. This modification proved effective in reducing the back reflection (glare) problem. The images show that the current system has adequate lighting for the darkest soils.

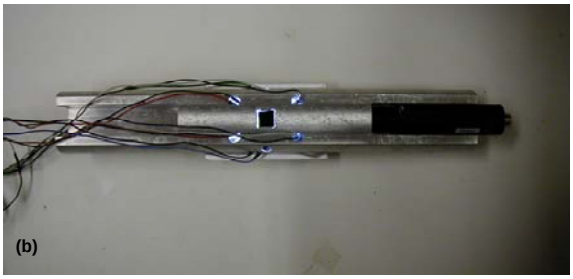

Figure 16**.** New dual camera module showing (a) window-side of the probe, and (b) camera side of probe.

More importantly, there is no glare or back reflection of the LED's from the window so the new design solves one of the major issues with the first generation of the GeoVis module.

Figure 17a and Figure 17b show images of Emory cloth captured with the dual camera system. For these images, the sapphire window was removed for the image capture because of the glare problem discussed previously. One camera was set up for a 6.4-mm wide FOV, whereas the other was set up for a 1.6-mm wide FOV. Both cameras were set to output s-video. The narrow FOV lens is an Infinistix of 44 mm focal length and 2X magnification, used with a 2X doubler tube, for a total magnification of 4X. The other lens is an Infinistix of 68 mm focal length and 1X magnification. The capture hardware used for the video microscope images is a Plextor ConvertX PX-M402U, an external USB 2.0 video capture device. Figure 17b and Figure 17c show images of a millimeter scale photographed at the two different fields of view as a measure of the width of the field of view (FOV) of the two camera systems.

Figure 18 shows images collected under conditions identical to those in Figure 17. Images are 60, 120, 180, 240 grit Emory cloth. Figure 19a shows the image of millimeter scale for the 6.4-mm and 1.7-mm fields of view. Figure 19b shows the corresponding millimeter scale for 1.7 mm field of view. Figure 20 shows digital images with the dual-camera system to test lighting and resolution at a 1.7-mm field of view. In this case images were captured of 60 grit Emory cloth, 120 grit, 180 grit, 240 grit Emory cloth.

Figure 21 show images of sandy soil from just outside the SPAWAR laboratory. For these images, the positions of the camera and lens were adjusted to provide greater magnification (smaller FOV). Otherwise the objects used for the images are the same. The black Emory cloth provided a worst case test for checking for adequate lighting levels. It is unlikely that the soils to be imaged will be as dark as the black Emory cloth. The 6.4-mm FOV shows good resolution allowing for accurate particle segmentation. Owing to the large particle sizes, the 1.7-mm FOV produces a somewhat blurred image of the larger particles but would be expected to provide sharper images of sediments in the very fine sand and silt fractions.

(a)

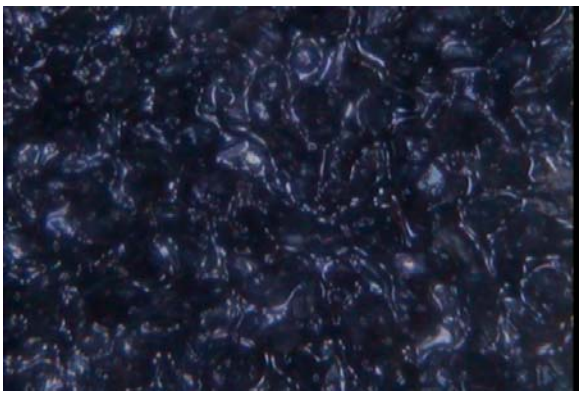

(b)

(c)

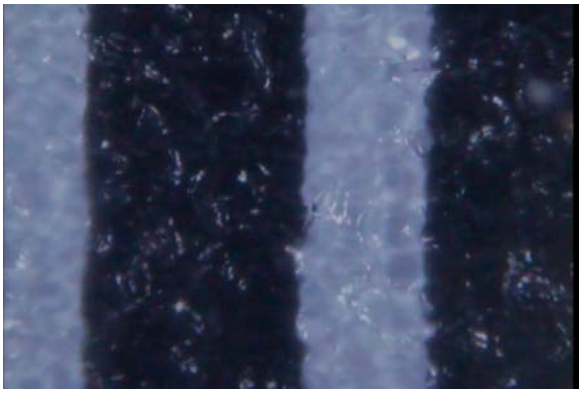

(d)

Figure 17**.** Digital images of used to test lighting and resolution, (a) 120 grit black sand paper photographed with the narrow field of view camera, (b) 120 grit black sand paper imaged with the wide field of view camera, (c) millimeter scale imaged with the with narrow field of view camera.

(a)

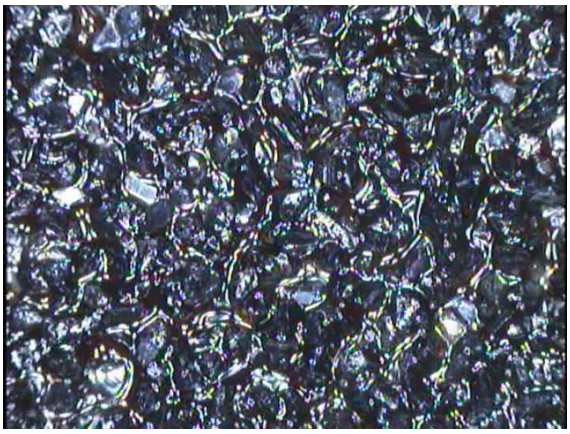

(b)

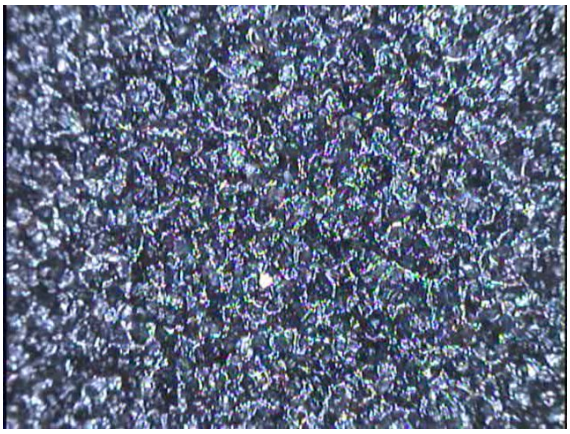

(c)

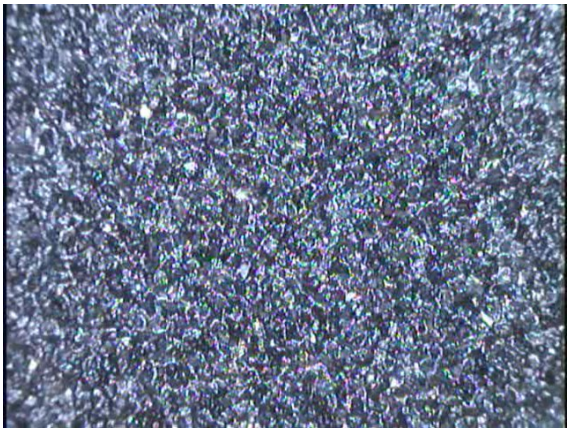

(d)

Figure 18**.** Digital images with the dual-camera system to test lighting and resolution at the a 6.4 mm field of view, (a) 60 grit Emory cloth, (b) 120 grit Emory cloth, (c) 180 grit Emory, and (d) 240 grit Emory cloth.

(a)

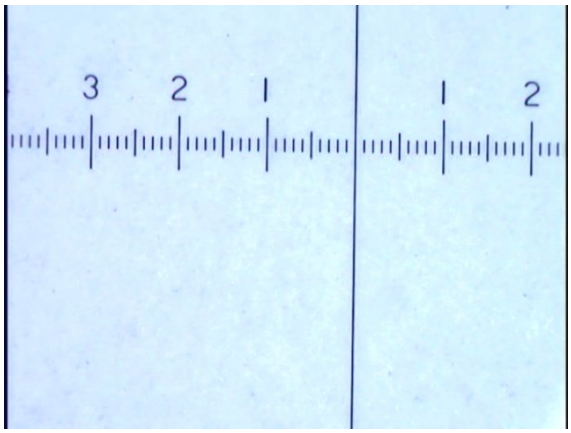

(b)

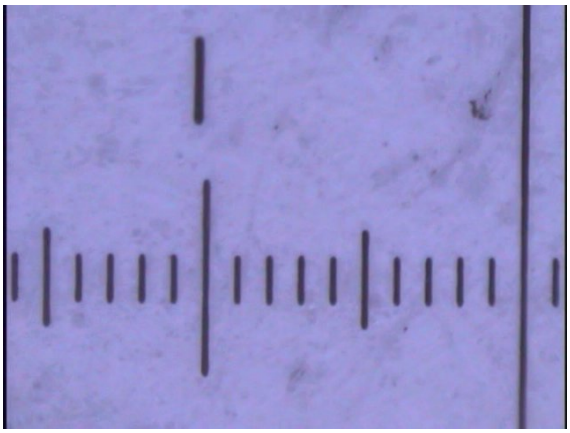

Figure 19**.** Digital image of millimeter scales for (a) 6.4 mm field of view and (b) 1.7 mm field of view.

The modified GeoVis probe appears capable of resolving textural changes, even under poor background lighting conditions. Direct push optical methods could easily provide real-time high-resolution images useful for differentiating soil characteristics based on texture information. The next step was to test the system with actual soils.

Figure 22 show images of soil-color samples from the University of Arizona Soil Club. These soils have ID numbers #3, #4 and #17 (U of A's numbering system). Figure 23 show images of soil-color samples from the University of Arizona Soil Club. These soils have ID numbers #7, #15 and #1 (U of A's numbering system). Each soil was photographed twice, once with the narrow FOV camera (1.6mm wide FOV), and once with the wide FOV camera (6.4mm wide FOV). Note that the images photographed with the narrow FOV had a reticle placed on top of the soil for reference. Samples were prepared by placing a quarter teaspoon of a given soil sample into a small plastic dish. A square piece of standard microscope slide glass was placed on top of the soil sample and tamped down. This was placed under the lighting fixture that was machined to go into the soil probe. The Sony XC-555 video camera, along with a Pinnacle Systems Movie Box video converter with USB interface, was used to capture the images. Two different InfiniStix lenses were used with this camera. The first lens (44 mm focal length, 2X magnification) was used together with a 2X doubler tube, for a total magnification of 4X. The other lens (68 mm focal length, 1X magnification) was used without the doubler tube. There are 2 images each of the three soils, one taken with the narrow FOV camera (1.6-mm wide FOV), and the other with the wide FOV camera (6.4-mm wide FOV). Colors inferred from the images were consistent with those defined by the Munsell color chart designations for the soil standards suggesting good color resolution with the dual camera system.

Following the successful completion of the laboratory testing, the camera module was installed into the SSC-CD SCAPS truck and integrated it into the existing hardware. Some hardware upgrades were required; specifically the data acquisition computer had to be upgraded to have a USB 2.0 for the MPEG 2 video capture device. The existing SCAPS system could only capture MPEG 1 video. Thus, a new USB MPEG 2 video capture device was integrated with the video system and tested with the closed caption encoder system.

(a)

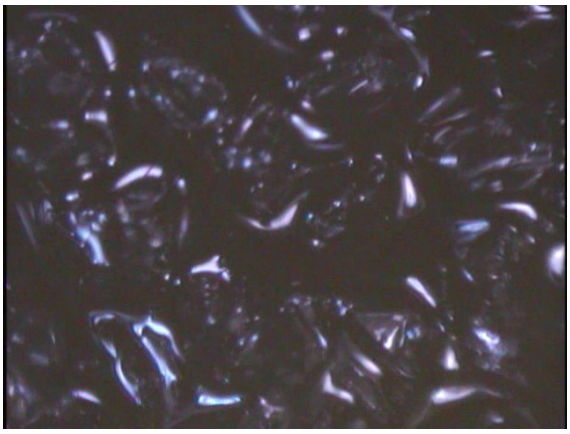

(b)

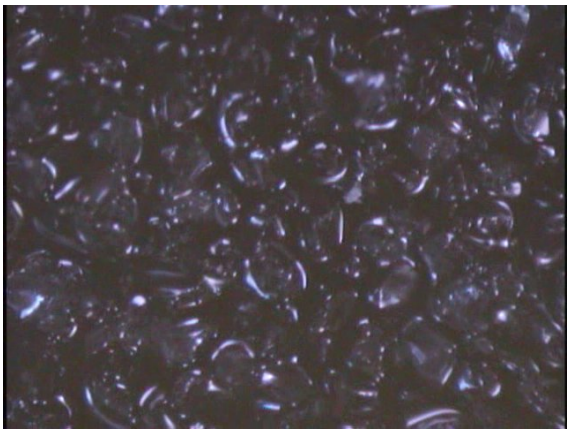

(c)

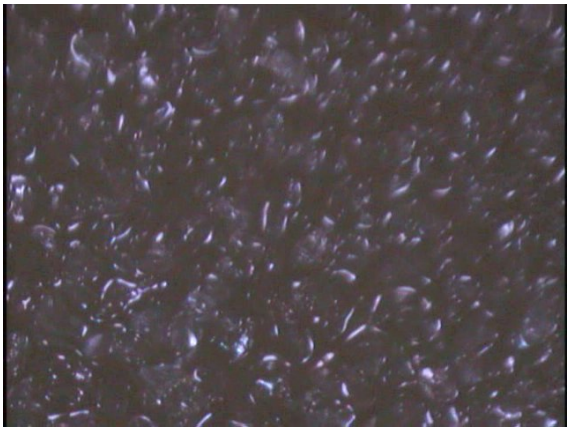

(d)

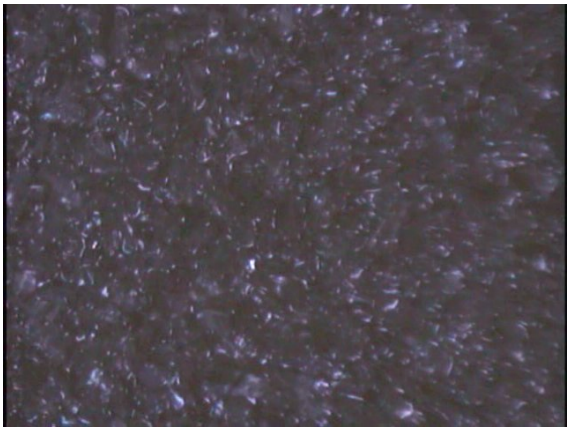

Figure 20**.** Digital images with the dual-camera system to test lighting and resolution at a 1.7-mm field of view, (a) 60 grit Emory cloth, (b) 120 grit Emory cloth, (c) 180 grit Emory cloth, (d) 240 grit Emory cloth.

(a)

(b)

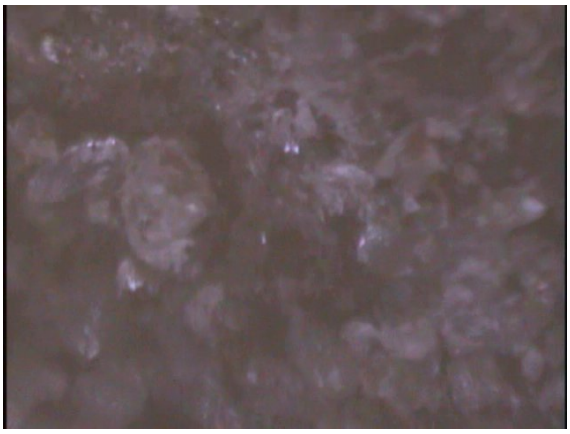

Figure 21**.** Digital images with the dual-camera system to test lighting, (a) sand soil at a 6.4-mm field of view, and (b) sand soil at a 1.7-mm field of view.

(a)

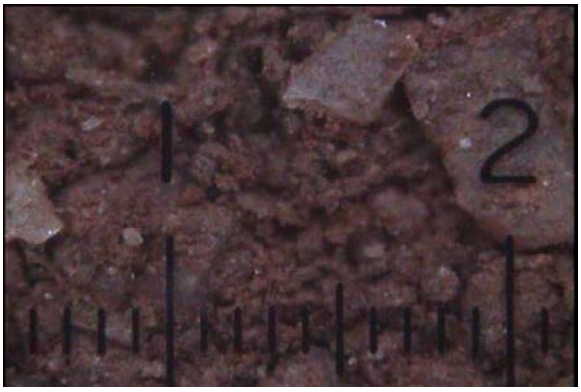

(b)

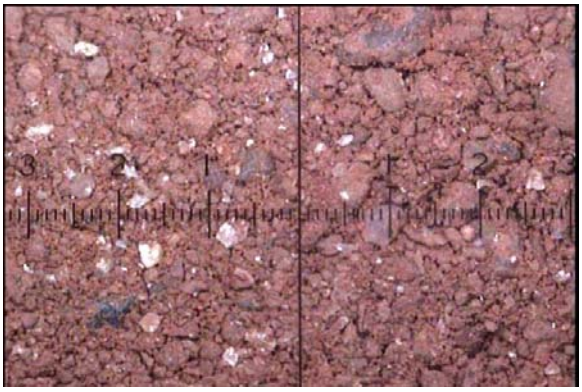

(c)

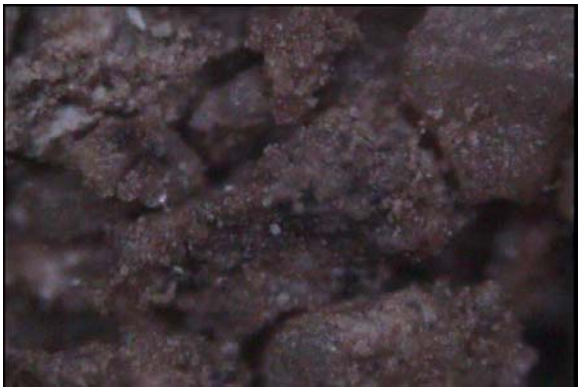

(d)

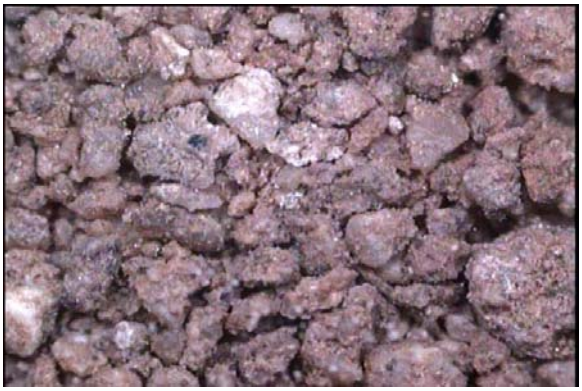

(e)

(f)

Figure 22**.** Digital images samples from the University of Arizona Soil Club used to test color resolution, (a) soil #3 at 1.6-mm field of view, (b) soil #3 at 6.4-mm field of view, (c) soil #4 at 1.6-mm field of view, (d) soil #4 at 6.4-mm field of view, (e) soil #17 at 1.6-mm field of view, (f) soil #17 at 6.4-mm field of view.

(a)

(b)

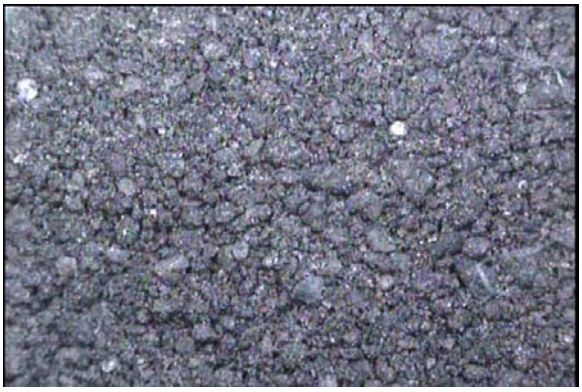

(c)

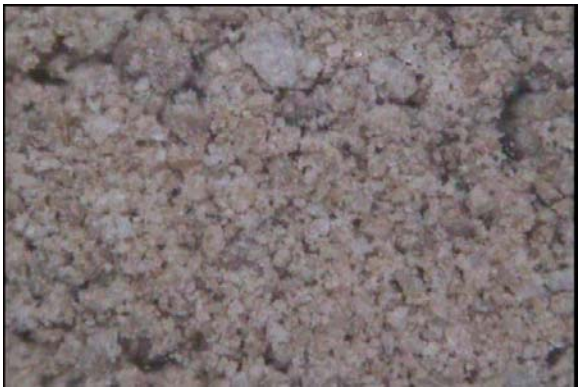

(d)

(e)

(f)

Figure 23**.** Digital images samples from the University of Arizona Soil Club used to test color resolution, (a) soil #7 at 1.6-mm field of view, (b) soil #7 at 6.4-mm field of view, (c) soil #15 at 1.6-mm field of view, (d) soil #15 at 6.4-mm field of view, (e) soil #1 at 1.6-mm field of view, (f) soil #1 at 6.4-mm field of view.

In anticipation of the system upgrade, discussions have been initiated with the software developer that produced the SCAPS data acquisition software about integrating the new photogrammetric processing software into the current WinOCPT software system. The vendor was unwilling to provide the source code and options for integrating the software were then explored. The available options included provision of the PNNL-developed software provided as a Dynamic-Link Library (DLL) that could be called from the SCAPS code, providing the PNNL source code to vendor compile as part of the SCAPS code, or to run the PNNL-developed code independently of the SCAPS code, either in the background, waiting for the image files to appear in a specific directory, or post processing the images. After exploring these options, it was determined that the preferred method of interfacing with the SCAPS WinOCPT software would through a standalone application that could be configured to search for new image files in specified directories to automatically process the new files as they are created. The output of the program is a text file with the porosity data as well as an image file of the processed image. A supplemental program was written to work with the SCAPS software, WinOCPT, to display to the user the output of the PNNL program. The data are then displayed in a window along with the processed image. The PNNL code runs independently of the WinOCPT application and so the same application can be used for post processing the image files if necessary.

The process of installing the new probe in the SSC-SCAPS System became somewhat more involved than expected as many components had to be upgraded to be compatible with the new image system, in particular the capture computer, and to be compatible with the PWC SCAPS System (the end users). To facilitate the transition from the laboratory test setup to the field installation, a contractor was used to facilitate the installation of the new system and to operate the SCAPS System. Nonetheless, these tasks were completed in a timely fashion and field testing initiated.

Figure 24 through Figure 32 show the end results of this task. Figure 24 shows the completed dual-camera probe as mounted in the cone penetrometer shaft. The small hole to the right of the sapphire window is a set screw that holds the internal assembly in place. Figure 25 shows part of the cables that connect to the umbilical to provide power and s-video transmission capabilities at the rod end of the camera probe. Figure 26 is a picture of the dual-camera probe inner assembly showing the probe end of the power and s-video cable and part of the 200-ft umbilical. Figure 27 shows the completed dual video probe being installed in the push rod housing. Figure 28 is a photograph of the probe stored in the rack on board the SCAPS truck in preparation for deployment. The push rods used with the probe are lined up to the left of the camera module. Figure 29 shows the probe in the hydraulic push fixture. The image capture computer is in the background. Figure 30 shows the probe positioned just above the ground, ready for ground penetration. In Figure 31, the outputs from both cameras are displayed; the upper image is from the 1.6-mm FOV camera, whereas the lower image is from the 6.4-mm FOV. These images represent simultaneous views of the same soil. Figure 32 is a screenshot of the complete system in operation. The SCAPS application (WinOCPT) is running as well as the PNNL-developed image processing code. The window at the lower left displays the output of PNNL's program, porosity data and the segmented image. The upper left window is the user interface for the WinOCPT program. This is typical of what the end user will see during operation. The system is complete, testing has been successful, and the improved system can be transitioned to the field use.

Figure 24**.** Completed dual-camera probe. The small hole to the right of the window is the set screw that holds the internal assembly in place.

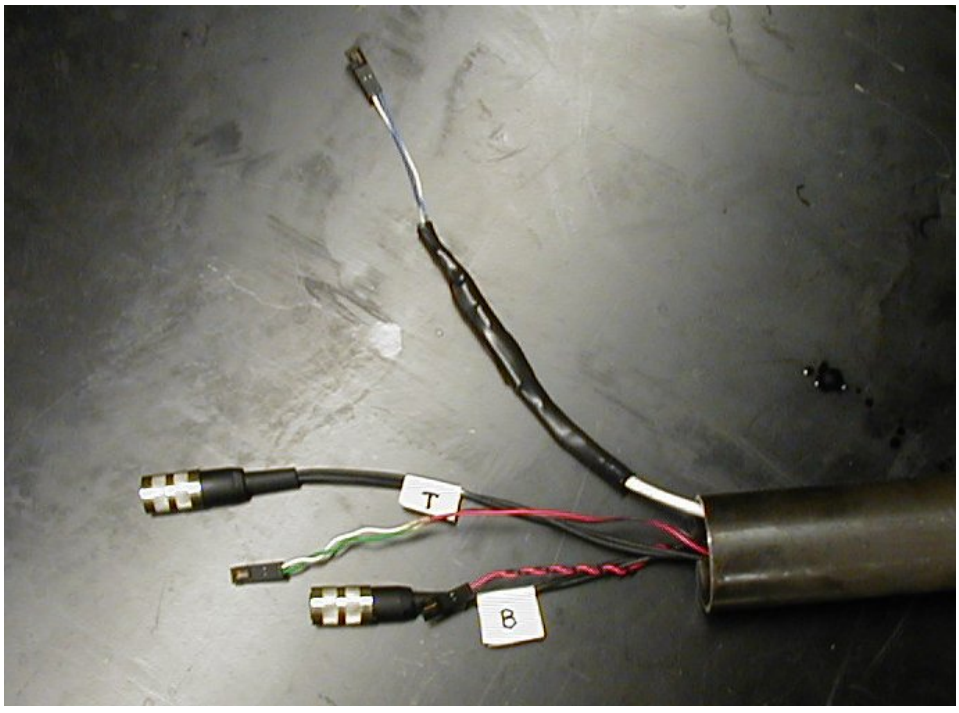

Figure 25**.** The cables for power and s-video at the rod end of the camera probe.

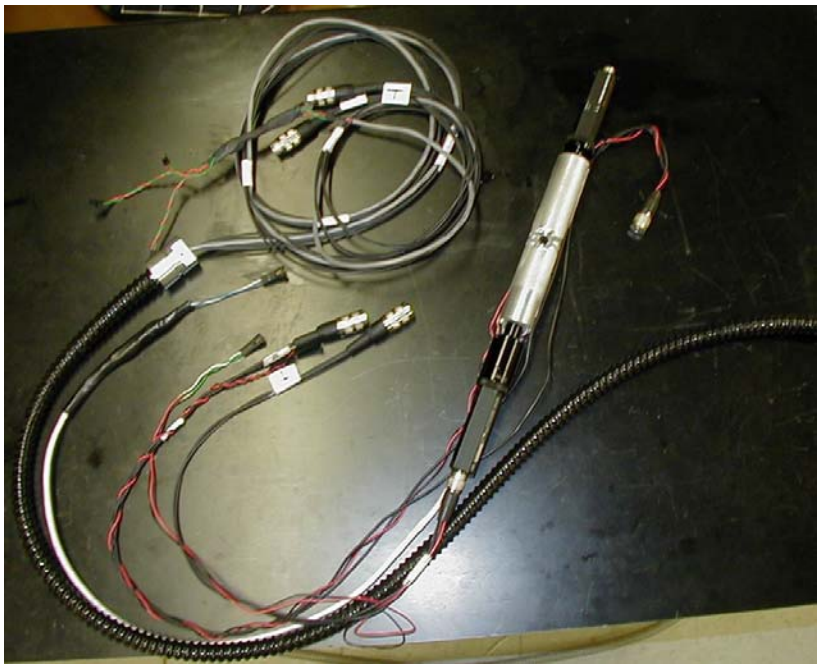

Figure 26. Dual Camera Probe inner assembly with the probe end of the power and s-video cable and part of the 200-ft umbilical.

Figure 27. Completed video microscope probe inside of housing.

Figure 28**.** Probe on rack in SCAPS truck prior to field testing.

Figure 29**.** Probe in hydraulic push fixure.

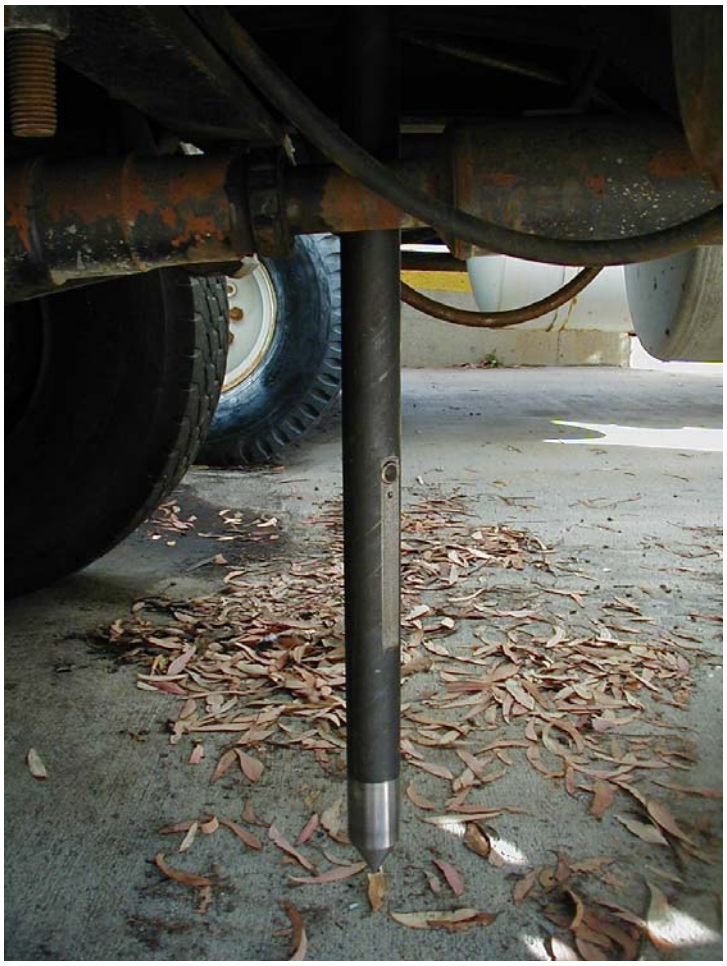

Figure 30**.** Probe in position ready for ground penetration.

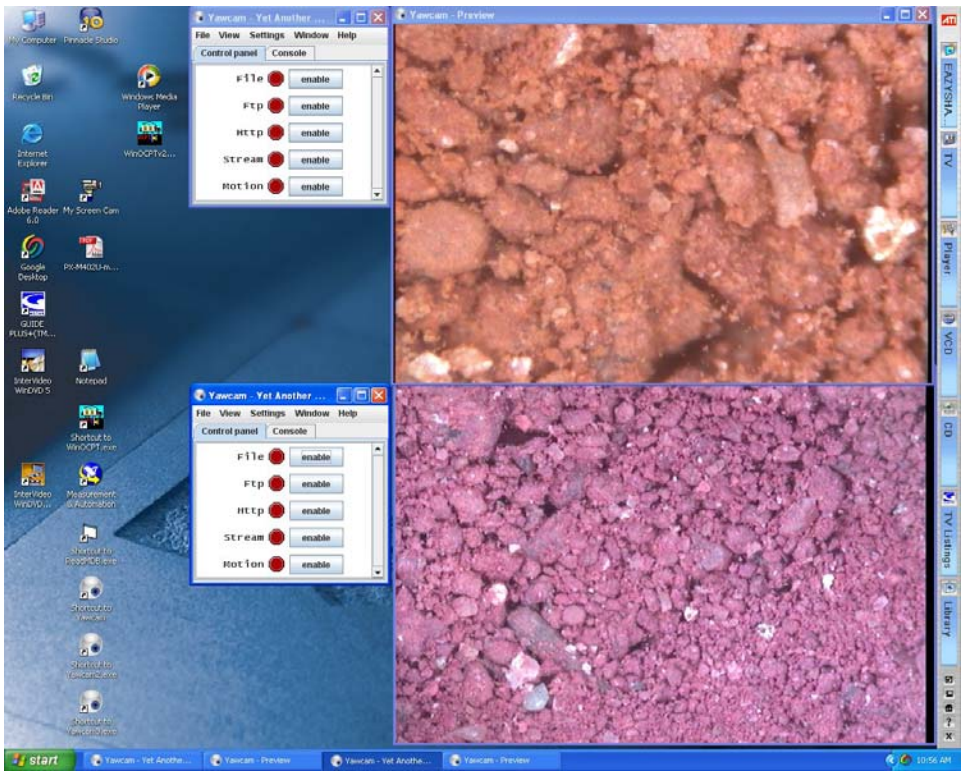

Figure 31. Screenshot of dual video views (1.6-mm and 6.4-mm fields of view) of sample soil.

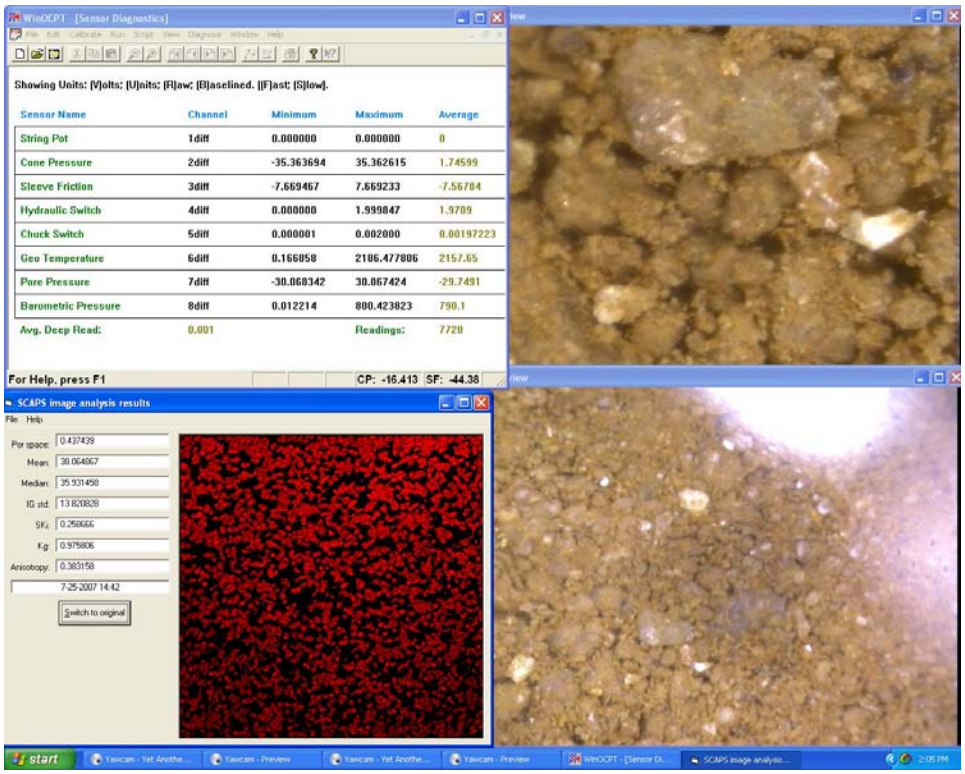

Figure 32**.** Dual Video with Porosity Window and WinOCPT Window

4.3 Photogrammetric Tools for Grain Size Characterization

After exploring several options, image-based measurement emerged as an affordable technology for information extraction and physical modeling of sediments. However, the information content of a sediment image is compounded and influenced by several factors such as illumination and local contrast differences, surface characteristics, and imaging sensor. These factors make the information retrieval from images a non-trivial task. The objective of this task was to develop the algorithms necessary to derive granulometric properties of the sediments from down-hole video images of lithostratigraphy obtained with the dual-camera microscope system. First, data quality objectives for the image analysis task were established to ensure that imaging system could provide data of sufficient quality. It was agreed that the use of segmentation for image-based measurement should address the following issues:

- Ability to adapt to the contrast variation across the image and to the spatial extent of different image features (feature size)
- Minimally affected by illumination differences
- Combine segmentation, classification, and measurement in a single step
- Should use an objective and automatic threshold to separate the objects of interest from their background
- Should cover multiple applications

Armed with these requirements, it became obvious that existing segmentation techniques would not be applicable to the complex problem of image-based measurement. The result was a general image-based approach for particle size distributions, referred to as the "Pixel-Vernier" (PV), combines markers-controlled watershed algorithm with a minimum-distance clustering to solve the segmentation problem. The combined algorithm is embedded in a coarse-to-fine strategy using a one training parameter to adapt the algorithm to different size distributions.

A series of experiments were conducted to demonstrate the validity and the generality of the proposed algorithm. The first set of the experiments were devised to show the computational accuracy of the algorithm and its predictive capability of ground truth information. The PV approach was used to estimate the mean, median, inclusive graphic standard deviation, inclusive graphic skewness, inclusive graphic kurtosis, and anisotropy for each image of the particle distribution. As stated previously, the accuracy of the segmentation or the particle regions delineation results is judged visually at the training stage. This training was achieved by searching for an optimal window size for the smoothing filter.

A Sony XC-555 microscopic digital video camera was used to acquire four images with known average distribution sizes (Figure 33). This camera was equipped with a fixed focal length, 6.4 mm, and it had an effective image size of 768 x 494 pixels. The average particle or grit sizes captured by each image are 53 μm, 78 μm, 116 μm, and 278 μm respectively. The spatial resolution of the four images was 10 μm/pixel. In other words, every pixel represents 10 μm. Figure 34 shows the results of the markers-controlled watershed segmentation on the image depicted in Figure 33a. The yellow boundaries highlight the particle regions at the coarse level. The local over-segmentation is very clear in each region, as shown by the zoom-in patches

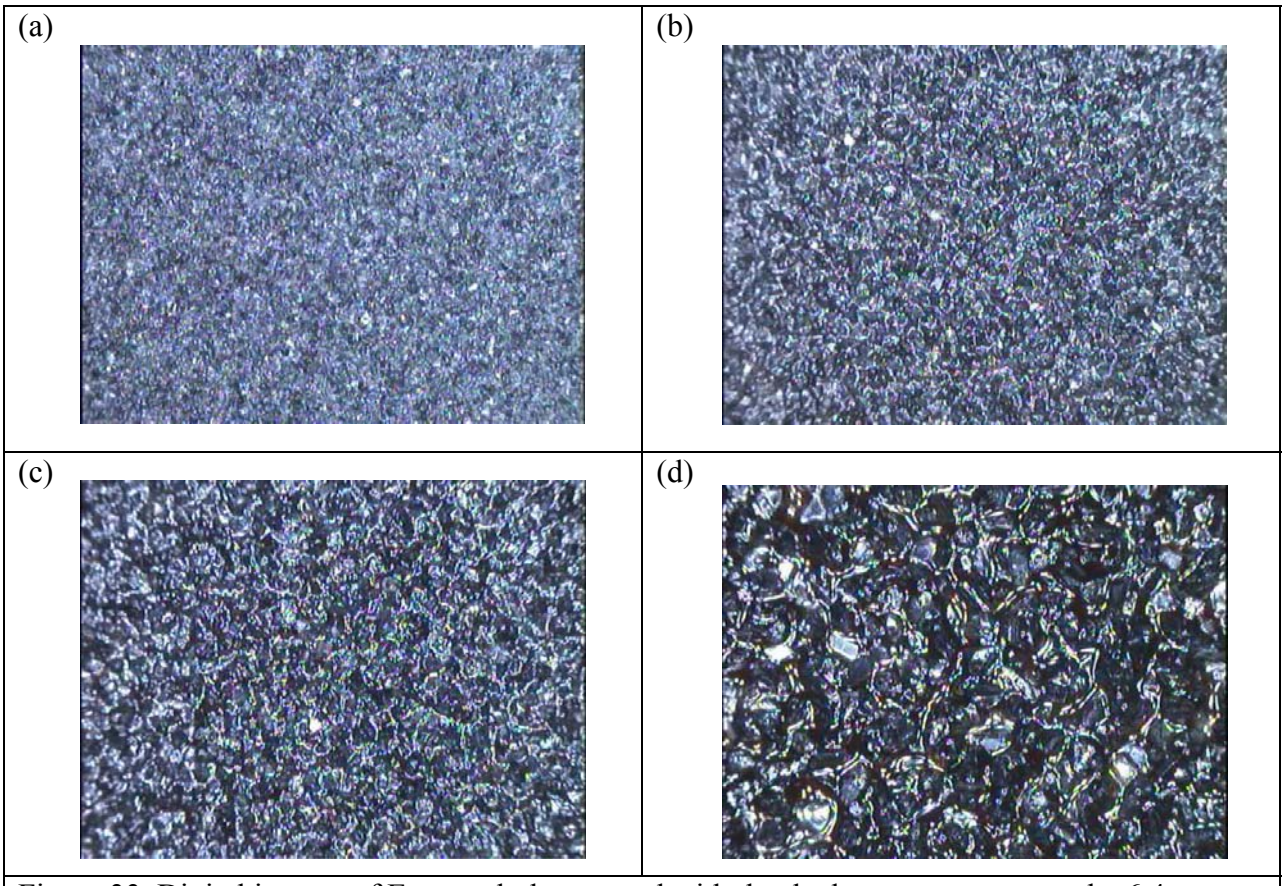

Figure 33**.** Digital images of Emory cloth captured with the dual-camera system at the 6.4 mm field of view (a) 53 μm grit size, (b) 78 μm grit size, (c) 116 μm grit size, and (d) 278 μm grit size.

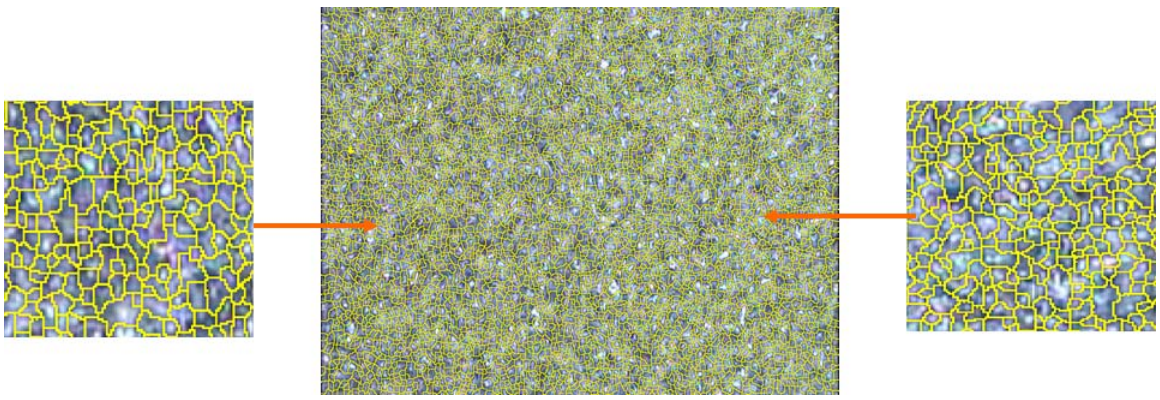

Figure 34**.** Markers-controlled watershed segmentation for the image shown in Figure 33a.

appeared to the left and the right. This result and the others obtained in different experiments, but not reported here, justify the use of the minimum distance clustering algorithm to refine or to delineate the optimal region. Figure 35 shows the binary images for the results of the minimum distance clustering and the white regions refer to the delineated particles. Figure 36 shows the cumulative distributions for the diameters of the particle images displayed in Figure 35.

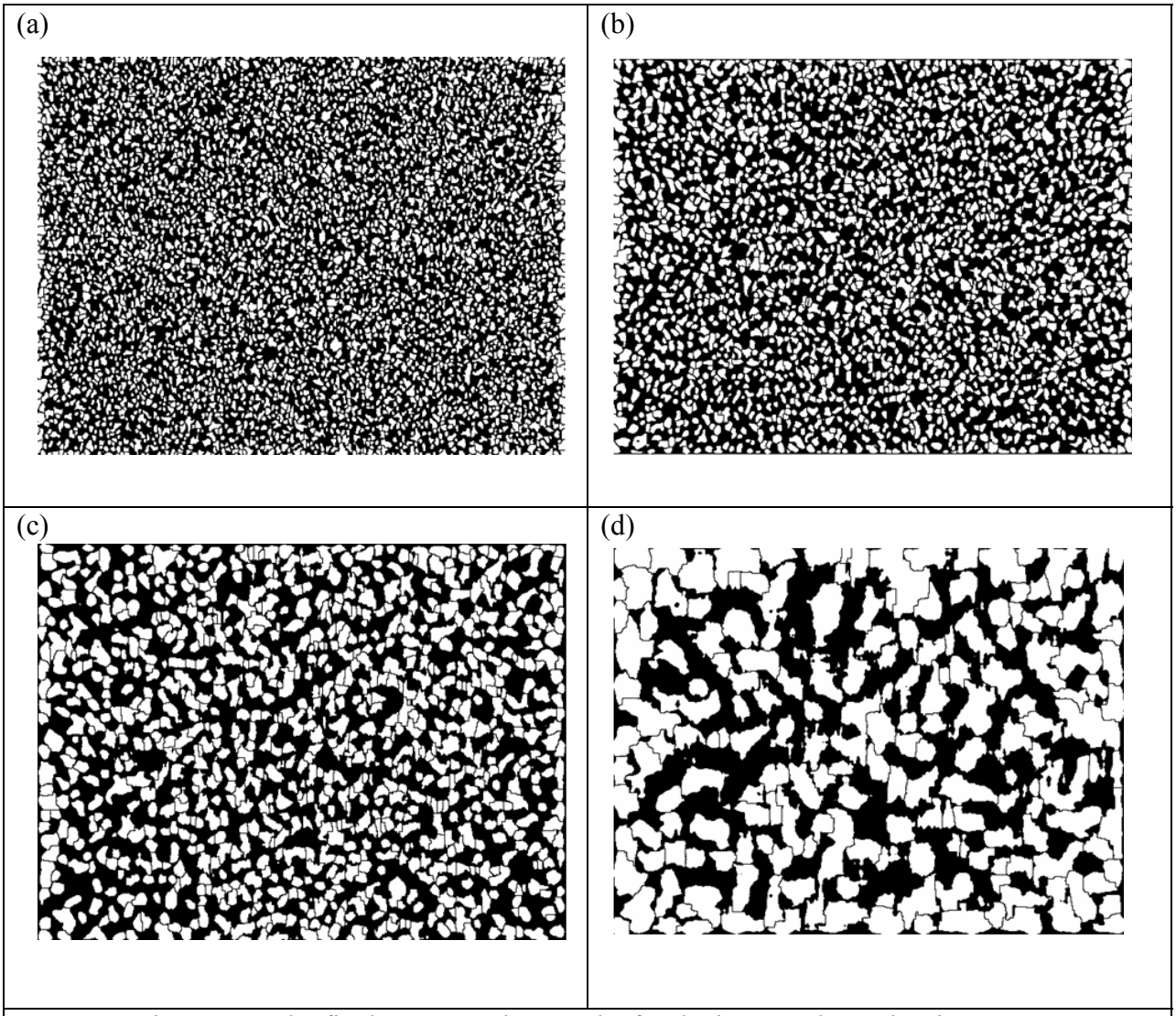

Figure 35. The final segmentation results for the images shown in Figure 33.

(a)

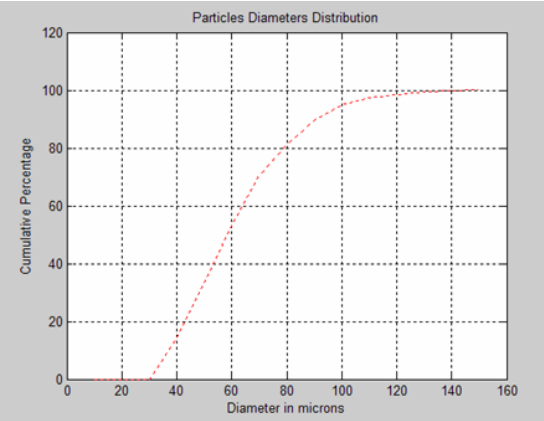

(b)

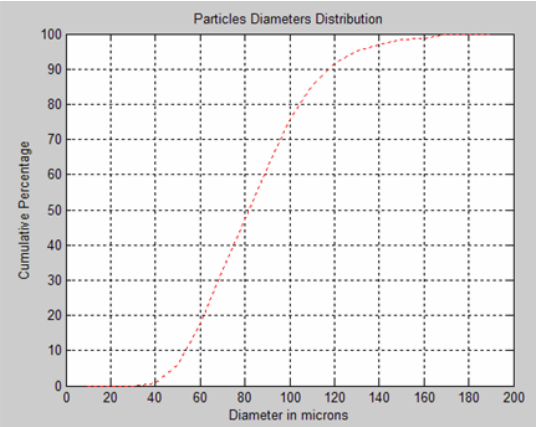

(c)

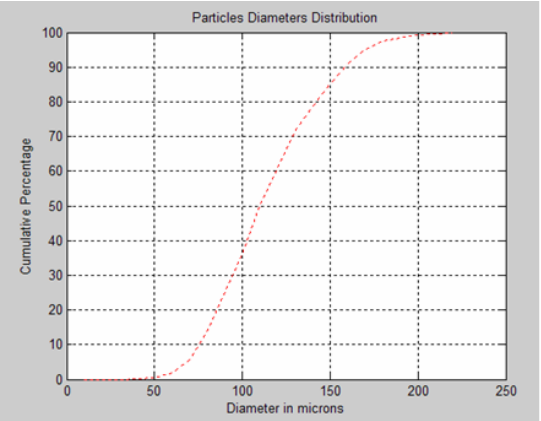

(d)

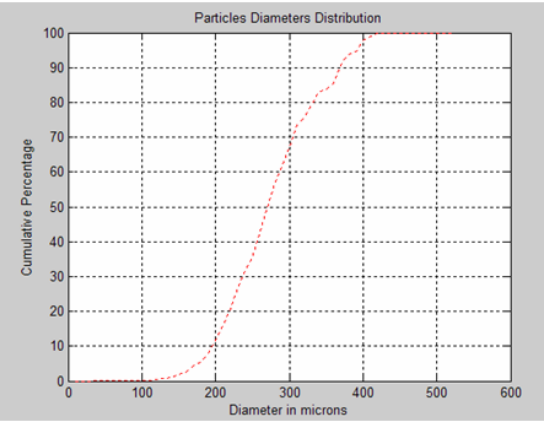

Figure 36. The particle size distribution for images shown in Figure 33.

Table 3 shows the estimated statistics for the particle distribution of the images shown in Figure 33. The second column in Table 3 and the rest of the columns depict the actual average values for the particles associated with each image. The results shown in Table 3 confirm that the developed algorithm reproduces the actual mean diameters for the four distributions and with a very small deviation in images B and C. The selection of the optimal window size for the averaging filter, as shown in Table 3, is very robust in the sense of not being very close to the actual value of the diameter. In addition, the closeness between the mean and the median is a strong indicator that the average mean diameter is a representative measure for the whole distribution captured by the image since this closeness can be interpreted as unbiased mean diameter. The last column of Table 3 shows the anisotropy as computed by equation 24, which is a very hard measure to get by normal sieving. In addition, the deviation of the anisotropy from zero clearly defeats any hypothesis for sphericity or isotropy.

Table 3. The estimated statistics for the images shown in Figure 33.

Image	Mean Diameter (μ)	Window Size	PV Mean Diameter (μ)	PV Median Diameter (μ)	σ_I	SK_I	K_G	Anisotropy
A	53	3	53.03	53.64	16.41	-0.137	1.111	0.376
B	78	5	73.40	73.70	16.77	-0.055	0.836	0.354
C	116	7	113.4	115.63	31.87	0.162	0.929	0.360
D	278	17	277.9	270.19	68.65	0.150	0.993	0.354

The algorithm was evaluated to determine its applicability to general particle patterns with a manually obtained ground truth. Figure 37a shows an image of a snake skin pattern. The manual measurement of the average diameter for the texture elements is 9.5 ± 1 pixels. Figure 37b shows the final segmentation results whereas and Table 2 presents the relevant parameters estimated by PV. From the results in Table 4 it is evident that the proposed PV algorithm provides a very close estimate for the average diameter (10.731 pixels) in light of its ground truth value (9.5 pixels). Although the algorithm resulted in incorrect segmentation in terms of lumping together some texture elements as a single object (see Figure 37b), the final result of the average diameter is impacted very slightly and this is because there are enough correct segmentation results that make the impact of incorrect ones almost negligible. As in the case of the Emory cloth analysis the particles, which appear circular, show evidence of anisotropy but to a lesser extent than in the Emory cloth images.

Given that the main application of interest is the segmentation of soil and sediment images, another set of tests were conducted using an image of gravel (Figure 38a). The objective of this experiment was to investigate the applicability of the algorithm on a natural sediment, the results if which would be of great practical value to a variety of engineering and scientific fields. The quality of particles delineation is used as a metric or ground truth to judge the performance of the PV algorithm as the true particle size moments are unknown. Figure 38b shows the final results

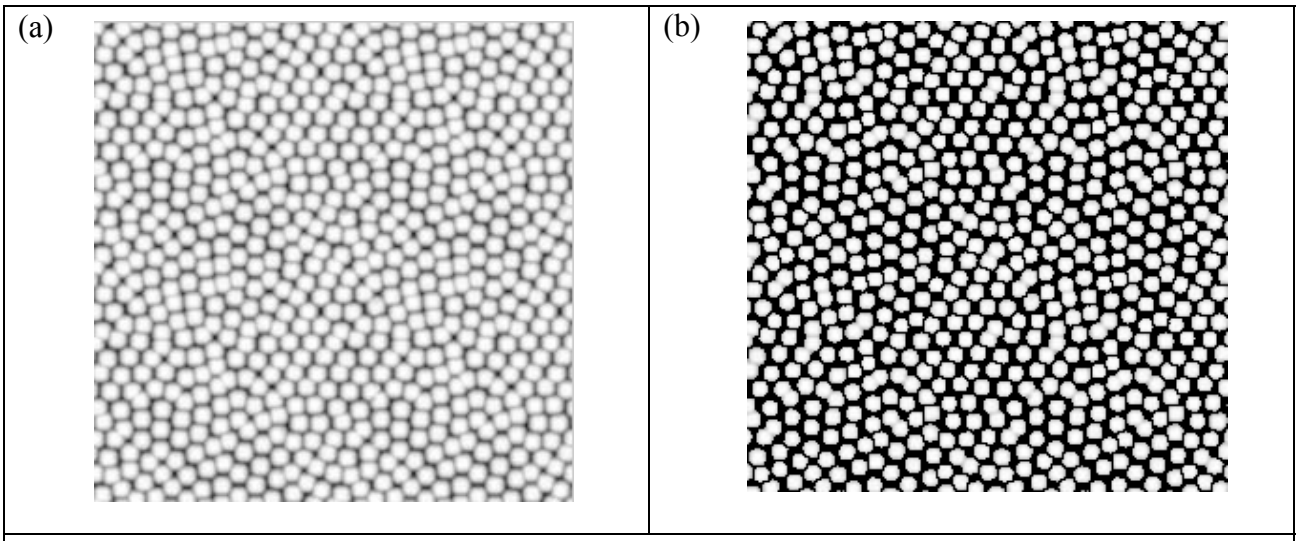

Figure 37. Digital image of a snake skin pattern, (a) original image, and (b) image segmented using the PV algorithm.

Table 4. The estimated statistics for the snake skin image

Image	Mean Diameter (μ)	Window Size	PV Mean Diameter (μ)	PV Median Diameter (μ)	σ_I	SK_I	K_G	Anisotropy
Snake	9.5 ±1	5	10.731	8.101	0.490	-1.912	1.4381	0.251

of the segmentation obtained from the PV algorithm. The segmentation results shown in Figure 38 confirms that the proposed algorithm can separate the information content of the image (here: pixel intensities) into meaningful objects (here rocks). Table 5 summarizes the grain size moments derived from the image using the PV algorithm. The closeness between the mean and the median is a strong indicator that the mean diameter is representative measure for the rock distribution as captured by the image. The robustness of the widow size of the averaging filter in terms of its relationship to the estimated mean diameter or the median is also worth noting. In other words, this window size does not have to be exact to get meaningful results. The anisotropy of the rocks distribution is also captured by the PV algorithm and is estimated 0.323. The common value of the shape factor (ψ) for natural soil and sediment particles is around 0.70, which is equivalent to an anisotropy ratio of 0.3 (i.e., 1- ψ) as defined in equation 24.

A similar analysis was performed on an image captured by the Mars Rovers (from Mars data; see Figure 39a. This is a microscopic image taken by the Mars Exploration Rover Spirit. The metric resolution of this image is 30 μm/pixel. In particular, this image shows a dominant cluster of coarse grains in the distribution. The purpose of this test was to show the generality of the algorithm on an atypical data set and to support the diversity argument claimed as an advantage

(a)

(b)

Figure 38. Digital image of gravel sediment, (a) original image, and (b) image segmented using the PV algorithm.

Table 5. The estimated statistics for the gravel image

Image	Mean Diameter (μ)	Window Size	PV Mean Diameter (μ)	PV Median Diameter (μ)	σ_I	SK_I	K_G	Anisotropy
Rock	Unknown	17	32.983	34.648	7.585	-0.268	0.925	0.323

(a)

(b)

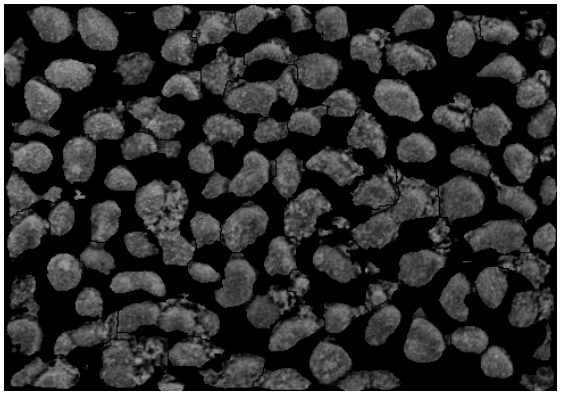

Figure 39**.** Digital image of sediment from Mars, (a) original image, and (b) image segmented using the PV algorithm. Image courtesy of NASA/JPL/Cornell/USGS.

Table 6. The estimated statistics for the Mars image

Image	Mean Diameter (μ)	Window Size	PV Mean Diameter (μ)	PV Median Diameter (μ)	σ_I	SK_I	K_G	Anisotropy
Gravel	Unknown	15	984.93	978.12	161.94	-0.029	0.968	0.339

of this approach. Again the visual check of the results is used as a metric to judge the quality of the segmentation. The segmentation results shown in Figure 39b confirm the robustness of the PV algorithm in terms of separating the particles from their background. The semi-identical values for the mean and the median are a strong indicator that the mean diameter can serve as a representative measure for the particles cluster distribution. As in the previous tests, there is evidence of anisotropy in this distribution with an estimated value of 0.339.

This task resulted in the development of a novel and general algorithm, the Pixel-Vernier, for particle size segmentation and the estimation of moments. The PV algorithm extracts particle size information a coarse-to-fine or global-to-local strategy. The markers-controlled watershed and smoothing provide the global extraction which is then refined by the minimum distance clustering algorithm. The PV generates results that are very comparable with their ground truth.

4.4 Porosity and Hydraulic Conductivity from Grain Size Distribution

Accounting for grain-scale heterogeneity on flow-and-transport properties requires an understanding of the properties of each soil fraction and how each fraction contributes to bulk

properties. Most packing models are based on the assumption of spherical particles but there is substantial evidence that particles in natural soils are aspherical, which can affect both porosity and hydraulic conductivity. This may explain the difficulty in predicting porosity and permeability from textural information. Although porosity is perhaps one of the simplest parameters for characterizing the packing of soil particles, accurate measures are very difficult to obtain for unconsolidated, poorly sorted sediments. This is partly because the process of sample collection often disturbs the structure. Predictions from grain size require information particle diameter and sorting but these are typically not reported in tests to derive textural class. In the sections below, predictions of porosity and hydraulic conductivity using particle shape and size distributions derived from photogrammetric methods are summarized.

4.4.1 Particle Shape

After particle diameter, particle shape is the second most significant sediment property in natural sediments. Thus, a critical step in estimating hydraulic properties from particle size distributions is the characterization of particle shape. To understand the relationship between particle size and shape, sediments were separated on 1ϕ intervals on the Udden-Wentworth particle-size scale and the lengths of the major, minor, and semi-minor axes determined using calipers (gravel fractions) and image analysis methods (sand and silt fraction). Axes lengths were used to calculate the, the anisotropy ratio, according to Eq. 24, and these are summarized in Table 7. In this scheme, anisotropy varies between 0 and 1, with a perfectly spherical particle having a value of 0. Essentially none of the particles are spherical. The smallest value (0.3432) is observed in the coarse sand fraction. For mean diameters less than 0.75 mm, the anisotropy increases with decreasing diameter. The same applies for particles larger than 0.75 mm with anisotropy initially increasing to a plateau before decreasing slightly. These data are critical for calculating porosity and hydraulic conductivity from particle size distributions as the parameters are very sensitive to particle shape

Table 7. Measured particle shape parameters for size fraction from natural sediments

Fraction	d_u (mm)	d_l (mm)	d_{avg} (mm)	Anisotropy
Very Coarse Pebble	64	32	48	0.4842
Coarse Pebble	32	16	24	0.5178
Medium Pebble	16	8	12	0.4677
Fine Pebble	8	4	6	0.4040
Very Fine Pebble	4	2	3	0.3634
Very Coarse Sand	2	1	1.5	0.3515
Coarse Sand	1	0.5	0.75	0.3432
Medium Sand	0.5	0.25	0.375	0.3582
Fine Sand	0.25	0.125	0.1875	0.3724
Very Fine Sand	0.125	0.0625	0.09375	0.4154
Silt	0.0625	0.00390625	0.033203	0.4363
Clay	0.00390625	0.001953125	0.00293	0.4792

4.4.2 Porosity

Table 8 shows the diameter at the lower boundary (d_l) and upper boundary (d_u) of each size class as well as the mean diameter, d_{avg}, for each size fraction. The average value of porosities for poured, tapped, and vibrated are also summarized for each fraction in Table 8. As can be expected porosity decreased from the poured values to tapped to vibrated. The porosity of the size fractions increased with decreasing diameter in the sand fractions and smaller. The vibrated porosity, $\phi_{vibrated}$, increased from 0.449 m^3 m^{-3} in the very coarse sand fraction to 0.462 m^3 m^{-3} in the very fine sand fraction. The trend continued as particle size became smaller, increasing from 0.540 m^3 m^{-3} in the coarse silt to 0.724 m^3 m^{-3} in the clay fraction. The increase in porosity with decreasing diameter is consistent with observations in the powder technology literature where increases in porosity with decreasing size has been reported for particles less and 500 μm (Wakeman 1975; Yu et al., 1996a,b). The measured porosities of the gravel fractions initially increased with increasing particle diameter before becoming constant. The initial increase with increasing diameter is inconsistent with literature reports which suggest a constant value of around 0.40 m^3 m^{-3} for coarse fractions. The measured values are also somewhat larger than those reported. The difference between these values and published results may be due to particle shapes. Most of the data reported in the literature are for random packs for spheres. Porosities of spherical particle packs have been reported to range from 0.40 m^3 m^{-3} for loose or poured packs to 0.36 for dense random packs (German, 1989). Larger values, such as observed here can be expected angular particles because of a greater tendency for bridging.

Table 8. Measured Porosities for Size Fractions of Natural Sediments

Fraction	d_u (mm)	d_l (mm)	d_{avg} (mm)	ϕ_{poured}	ϕ_{tapped}	$\phi_{vibrated}$
Very Coarse Pebble	64	32	48	0.459	0.410	0.403
Coarse Pebble	32	16	24	0.474	0.424	0.417
Medium Pebble	16	8	12	0.471	0.427	0.427
Fine Pebble	8	4	6	0.429	0.376	0.376
Very Fine Pebble	4	2	3	0.409	0.360	0.360
Very Coarse Sand	2	1	1.5	0.485	0.468	0.449
Coarse Sand	1	0.5	0.75	0.515	0.481	0.471
Medium Sand	0.5	0.25	0.375	0.555	0.506	0.477
Fine Sand	0.25	0.125	0.1875	0.559	0.519	0.481
Very Fine Sand	0.125	0.0625	0.09375	0.570	0.494	0.462
Coarse Silt	0.0625	0.03125	0.046875	0.655	0.540	0.540
Medium Silt	0.03125	0.015625	0.0234375	0.660	0.628	0.607
Fine Silt	0.015625	0.0078125	0.01171875	0.704	0.643	0.627
Very Fine Silt	0.0078125	0.00390625	0.005859375	0.727	0.664	0.637
Clay	0.00390625	0.001953125	0.002929688	0.784	0.724	0.724

As shown in Table 7, the gravel fraction anisotropy values were significantly higher than the sand fractions and initially increased with increasing particle diameter. Fine particles are also aspherical and this is reflected in the increase in anisotropy and porosity with decreasing particle size as shown above.

Figure 40 compares the measured and predicted porosities of binary mixtures of glass beads (2, 5, 14, 50 mm), used to represent gravel, and 20/30 Accusand used to represent the fine fraction. Such binary mixtures are good models of poorly sorted sediments. The porosity of the end members (100% Accusand, 100% glass beads) is consistent with published values for random packs. As the concentration of fines (Accusand) in the mixture increased, there was a clear decrease in porosity until a minimum value, ϕ_{min}, was reached. Values of ϕ_{min} decreased with increasing diameter of the coarse fraction and so did the critical the fines content, c, at which the minimum occurred.

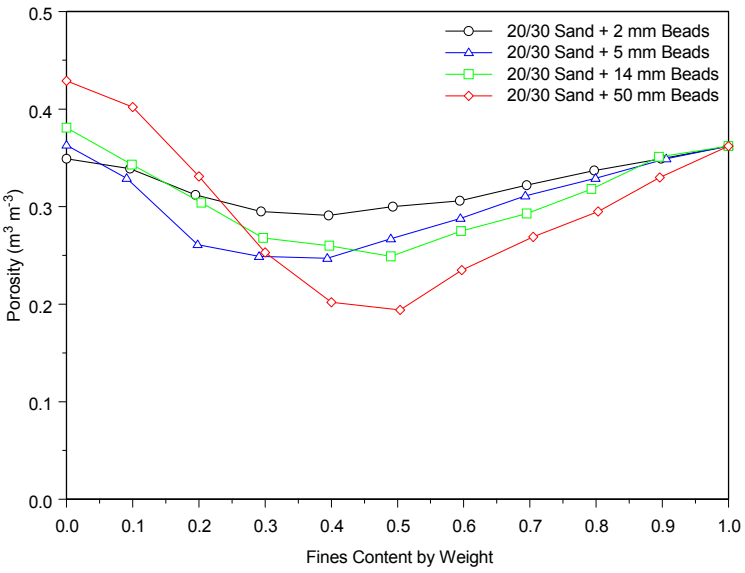

Figure 40. Porosity variation as a function of fines content in binary mixtures. The fine component is 20/30 Accusand whereas the coarse component is glass beads.

The observed ϕ_{min} decreased from around 0.30 m^3 m^{-3} with the 2 mm beads to 0.20 m^3 m^{-3} with the 50-mm beads. Following the occurrence of ϕ_{min}, porosity started to increase with increasing fines concentration. The observed decrease in porosity to a minimum value followed by an increase to the value of the finer end member is consistent with the fractional packing concept. Porosities predicted with the packing model described previously are also in good agreement with the measured values. The greatest challenge therefore in predicting the porosity of real sediment mixtures will be determining the relative amounts of fine and coarse fractions and determining the end-member porosities. Results of this work shows that complete grain size distribution curve can be readily obtained by photogrammetric techniques. End-member porosities can be derived from photogrammetric methods or from laboratory measurements on

soil fractions. Measurements such as those reported in Table 8 can be used to create databases for sediments with similar parent materials and depositional environments.

Using information on particle shape and porosities for end member fractions, the multicomponent packing model was used to predict the porosity of field samples collected from the immobilized low activity waste (ILAW) site at Hanford. Figure 41 compares the measured porosity with the porosity predicted based on the complete particle size distribution, the particle shape parameters and end member porosities for each fraction. The results are quite encouraging. These results suggest that relatively accurate predictions of porosity can be made if the component fractions are characterized.

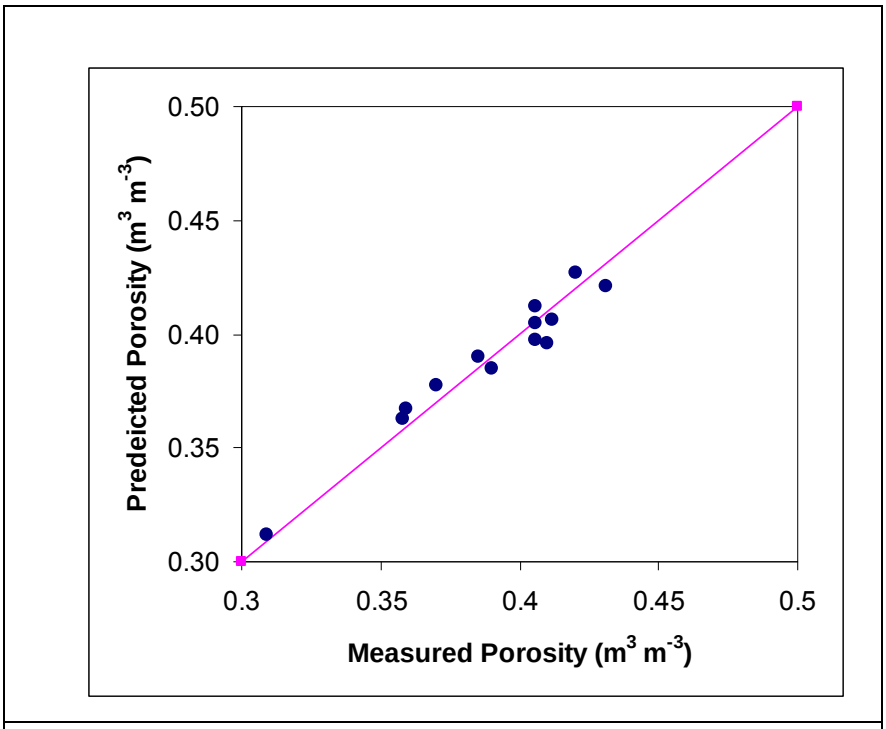

Figure 41. Comparison of porosities predicted from grain size distributions with measured porosities.

4.4.2 Hydraulic Conductivity

Figure 42 compares the measured and predicted hydraulic conductivities of the binary mixtures of glass beads (2, 5, 14, 50 mm) and 20/30 Accusand. The hydraulic conductivities of the end members (100% Accusand, 100% glassbeads) were consistent with published values for random packs and showed good correlation with mean diameter as predicted by empirical KC-type models. As with the porosity data, hydraulic conductivity decreased sharply from the value at 100% pure glass beads as the content of fines increased. This decrease is due to the mixture becoming less well sorted, with the fines filling the large pores formed by the coarser particles. Hydraulic conductivity reached a minimum, K_{min}, when the amount of fines became equal to the porosity of the coarse fraction. The most striking observation is that the relationship between K_s

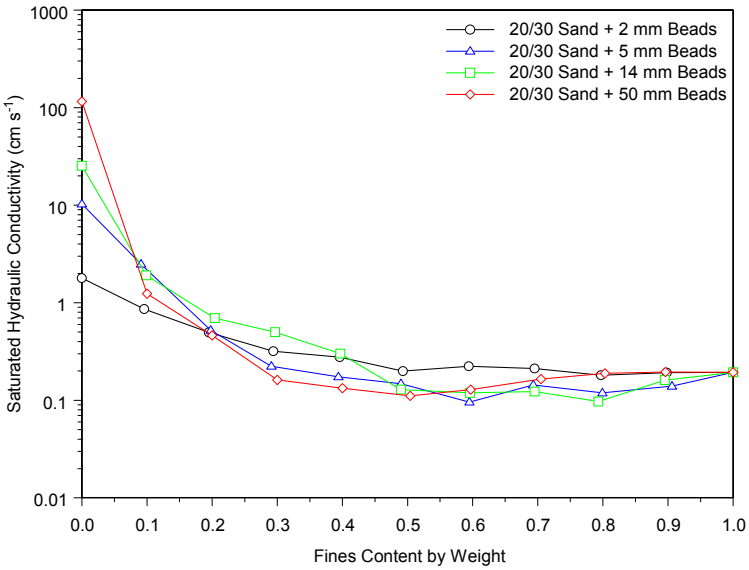

Figure 42. Hydraulic conductivity variation as a function of fines content in binary mixtures. The fine component is 20/30 Accusand whereas the coarse component is glass beads

and fines content is non-linear. This is inconsistent with widely used models that assume the ratio of K of the mixture to that of the fine fraction is equal to the ratio of the void ratio of the mixture to that of the coarse fraction. Such models predict a linear change in K_s as the concentration of fines increase.

5. Summary

The Pacific Northwest National Laboratory (PNNL), in collaboration with The Space and Naval Warfare Systems Center (SPAWAR) proposed to develop a rapid, robust and reliable tool for in situ measurement of hydraulic properties in heterogeneous, anisotropic, variably saturated porous media. To meet this objective, high-resolution subsurface imaging techniques were integrated with photogrammetric methods and subatmospheric hydraulic conductivity measurements to permit prediction critical hydraulic properties from cone penetrometer measurements.

A critical component of this project was the modification of the existing SCAPS/GeoVIS system to function as dual field-of-view video camera system for sub-surface soil imaging. This required modification of the single-camera GeoVis system to allow simultaneous capturing of images at different magnification factors to allow a more complete description of the grain size distribution curve. At each magnification, image-based grain size analysis is limited to those features that fall within predetermined limits. One camera is used to capture grain size data in the silt-sized fraction ($2 \leq d \leq 63$ μm) and the second to capture information in the sand-sized fraction ($63 \leq d \leq 2000$ μm). These two levels of magnification provide fields of view ranging from 2 to 20 mm diagonal. Digital imaging allowed automated recording of complex shapes in a controlled environment (scale, lighting, measurement) accurate to the level of a single pixel. Measurement in a digital environment also allows creation of ratios and proportional area measurements useful for lithofacies identification.

Digital images of the sediment were converted into particle size distributions and their moments using the Pixel-Vernier, a suite of photogrammetric algorithms that combine markers-controlled watershed algorithm with a minimum-distance clustering to solve the segmentation problem. The combined algorithm is embedded in a coarse-to-fine strategy using a one training parameter to adapt the algorithm to different size distributions. The segmentation algorithm decomposes the image into separate particle regions. These regions are used to derive several geometric attributes for each particle, such as the semi-major axis, the semi-minor axis, and the equivalent diameter. The geometric attributes of all the particles are used to estimate the particle size distribution and their relevant statistics. Particle size distributions were then used with a packing model to estimate porosity and saturated hydraulic conductivity which have the added benefit of constraining hydraulic conductivities derived from the borehole permeameter measurements. The approach proved successful in characterizing a diverse set of materials such as including soil, complex digital patterns, and sediment images from the Mars surface. The similarity between calculated and known parameters confirm the robustness of the algorithm in terms of separating the particles from their background and for deriving parameters, including particle shape parameters, that are currently not obtainable with traditional characterization methods.

Sediments were separated in 1ϕ fractions and characterized to determine particle shape, porosity and hydraulic conductivity. Binary mixtures of coarse and fine fractions were prepared using marbles, gravel, sand, and silt with the fine fraction ranging from 0 to 100% in increments of 10% . Measurements of particle shape, porosity and hydraulic conductivity were made on end members and mixtures to allow calibration of the Pixel-Vernier and a multicomponent packing model. Results show that particles in all the size classes are aspherical and that porosity end-member porosity increases with decreasing particle diameter in the sand fraction and smaller. In

the gravel fraction, end-member porosity initially increased with increasing diameter before becoming constant. A binary packing model was extended to the incomplete mixing of aspherical particles of all size classes and calibrated with laboratory measurements. Measured porosity and hydraulic conductivity both decreased to a minimum at a critical fines-content, much unlike the predictions based on complete mixing. Model results confirm that the mass-volume relationships and hydraulic properties are influenced by the fractional concentrations of each component.

A subatmospheric borehole permeameter proposed to overcome limitations in subsurface hydraulic conductivity measurements was successful in estimating hydraulic conductivities under laboratory and field conditions. Use of a subatmospheric pressure permeameter reduced the effect of macropores and fissures on matrix flow. For the analysis of data, a new method using the Brooks-Corey hydraulic model was developed to solve the steady-state infiltration equation. Results from numerical simulations compared with the results of laboratory experiments. Field measurements of unsaturated hydraulic conductivity were also in good agreement with independent measurements also the saturated conductivity was slightly underestimated. With the successful application of the packing model to the prediction of porosity and saturated hydraulic conductivity, the saturated conductivity can be easily constrained in the permeameter analysis.

This approach will lead to a better understanding of the measurements available for permeability characterization and help to establish the validity of permeability predictions in untested intervals based on measurements like grain size distributions that are easier to make. The data obtained using the direct push in situ sensors will be invaluable in the design and evaluation of environmental remedies.

6. References

American Society of Testing and Materials (ASTM). 2006. Standard Test Method for Permeability of Granular Soils (Constant Head). ASTM D2434-68, Philadelphia, Pennsylvania.

Allen, T., 1997. Particle size measurement: powder sampling and particle size measurement. Fifth edition, Vol. 1, Chapman and Hall: 525 p.

Amoozegar, A., 1989. A compact constant-head permeameter for measuring saturated hydraulic conductivity of the vadose zone. Soil Sci. Soc. Am. J. 53:1356–1361.

Bear J. 1972. Dynamics of Fluids in Porous Media. Dover Publications, Inc., New York.

Bright, D.S., and Steel, E.B., 1987. Two dimensional top hat filter for extracting spots and spheres from images. Journal of Microscopy, 146: 191-200.

Brooks, R.H., and A.T. Corey. 1964. Hydraulic properties of porous media. Hydrology Paper no. 3. Colorado State University, For Collins.

Butler, J., Lane, S., and Chandler, J., H., 2001. Automated extraction of grain-size data from gravel surfaces using digital image processing. J. Hydraulic Res, vol. 39 (4): 1-11.

Carsel, R., and R. Parrish. 1988. Developing joint probability-distributions of soil-water retention characteristics. Water Resour. Res. 24:755–769.

Carman, P.C. 1937. "Fluid Flow Through Granular Beds." Transactions of the Institution of Chemical Engineers, 15:150–166.

Carter, R., and Yan, Y., 2005. Measurement of particle shape using digital imaging techniques. Journal of Physics: Conference Series, 15: 177-182.

Chandler, M.A., Goggin, D.J., and Lake, L.W., 1989, A mechanical field permeameter for making rapid, non-destructive, permeability measurements: Journal of Sedimentary Petrology, v. 59, no. 4, p. 613-635.

Clarke RH. 1979. "Reservoir Properties of Conglomerates and Conglomeratic Sandstones." Am. Assoc. Pet. Geol. Bull. 63(5):799–809.

Clothier, B. E., and I. White, Measurement of sorptivity and soil water diffusivity in the field, Soil Sci. Soc. Am. J., 45, 241–245, 1981.

Diepenbroek, M., Martholoma, A., and Ibekken, H., 1992. How round is round? A new approach to the topic "roundness" by Fourier grain shape analysis. Sedimentology, vol. 39 (3): 411-422.

Elrick, D.E., and W.D. Reynolds. 1992. Infiltration from constant-head well permeameters and infiltrometers. In Advances in Measurement of Soil Physical Properties: Bringing Theory into Practice. SSSA Special Publication No. 30.

Folk, R., L., 1980. Petrology of sedimentary rocks. Hemphill Publishing Company, Austin, TX: 182 p.

Gardner, W. R., Some steady state solutions to the unsaturated moisture flow equation with applications to evaporation from a water table, Soil Sci., 85, 228–232, 1958.

German, R.M. 1989. Particle Packing Characteristics. In: Metal Powder Industries Federation, Princeton, N.J., 443 pp.

Ghalib, A., M. and Hryciw, R., D., 1999. Soil particle size distribution by mosaic imaging and watershed analysis, J. Comput. Civil Eng. vol. 13 (2): 80-87.

Gonzalez, R., C., and Woods, R., E., 2002. Digital image processing. Second edition, Prentice Hall: 793 p.

Graham, D., J., Rice, S., P., and Reid, I., 2005b. A transferable method for the automated grain sizing of river gravels. Water Resources Research, vol. 41: W07020.
Graham, D., J., Reid, I., and Rice, S., P., 2005a. Automated Sizing of Coarse-Grained Sediments: Image-processing procedures. Mathematical Geology, vol. 37 (1): 1-28.
Gribb, M. M., J. Šimůnek, and M. F. Leonard. 1998. "Development of a cone penetrometer method to determine soil hydraulic properties," ASCE Journal of Geotechnical and Geoenvironmental Engineering, Vol. 124, No. 9, 820-829, 1998.
Hussen, A. A., and A. W. Warrick, Algebraic models for disc tension permeameters, Water Resour. Res., 29, 2779–2786, 1993.
Hwang, S.I., K.P. Lee, D.S. Lee, and S. E. Powers. 2002. Models for estimating soil particle-size distributions. Soil Sci. Soc. J. 66:1143-1150.
Ibekken, H., and Schleyer, R., 1986. Photo-sieving: A method for grain-size analysis of coarse-grained unconsolidated bedding surfaces. Earth Surface Processes Landforms, vol. 11 (1): 59-77.
Itti, L., and Koch, C., 2001. Computational Modeling of Visual Attention, Nat. Rev. Neurosci. 2(3), pp: pages 194-203.
Kamann PJ, RW Ritzi, DF Dominic, and CM Conrad. 2007. Porosity and Permeability In: Sediment Mixtures. Ground Water 4594):429-438.
Kirkham, d., and W.L. Powers. 1972. Advanced soil physics. Wiley-Interscience, New York.
Koltermann, C. E., and S. M. Gorelick. 1995. Fractional Packing Model For Hydraulic Conductivity Derived From Sediment Mixtures, Water Resour. Res., 31, 3283–3297.
Korvin, G. 1982. Axiomatic Characterization of the General Mixture Rule. Geoexploration 19:267–276.
Kozeny J. 1927. Uber Kapillare Leitung Des Wassers Im Boden. Sitz. Akad. Wissensh, 136:271–306.
Lowry, W, N. Mason, And D. Merewether. 1999. Cone Permeameter™ – In-Situ Permeability Measurements With Direct Push Techniques. Waste Management'99 Conference, February 28 – March 4, 1999, Tucson, Arizona.
McEwan, I., K., Sheen, T., M., Cunningham, G., J., and Allen, A. R., 2000. Estimating the size composition of sediment surfaces through image analysis. Proc. Inst. Civil Eng., Water Maritime Eng., vol. 142 (4): 189-195.
McGeary, R. K. 1961. Mechanical Packing of Spherical Particles. J. Amer. Ceramic Soc. 44(10):513-522.
Meyer, F., and Beucher, S., 1990. Morphological segmentation. Journal of Visual Communication and Image Representation, Vol. 1 (1): 21-46.
Morton, K, S. Thomas, P. Corbett, and D. Davies. 2002. Detailed analysis of probe permeameter and interval pressure transient test permeability measurements in a heterogeneous reservoir. Petroleum Geoscience, Vol. 8 2002, pp. 209–216
Or, D., Shani, U., and A.W. Warrick. 2000. Subsurface tension permeametry. Water Resour. Res. 36(8):2043-2053.
Otsu, N., 1979. A threshold selection method from gray-level histograms. IEEE Transaction on Systems, Man, and Cybernetics, 9: 62-66.
Paillet, F.L., Cheng, C.H., and Pennington, W.D., 1992, Acoustic-waveform logging--advances in theory and application: The Log Analyst, v. 33, no., 3, p. 239-258.
Philip, J.R. 1987. Approximate analysis of the borehole permeameter in unsaturated soil. Water Resour. Res. 21:1025-1033.

Reynolds, W.D., and D.E. Elrick. 1991. Determination of hydraulic conductivity using a tension infiltrometer. Soil Sci. Soc. Am. J. 55:633-639.
Reynolds, W.D., and D.E. Elrick. 1990. Ponded infiltration from a single ring: I. Analysis of steady flow. Soil Sci. Soc. Am. J. 54:1233-1241.
Reynolds, W.D., D.E. Elrick, and B.E. Clothier, The constant head well permeameter: Effect of unsaturated flow, Soil Sci., 139, 172–180, 1985.
Reynolds, W.D. 1986. The Guelph Permeameter method for in situ measurement of field-saturated hydraulic conductivity and matric flux potential. Ph.D. dissertation. University of Guelph, Guelph, Ontario.
Russ, J., C., 2002. The image processing handbook. Fourth edition, CRC Press: 732 p.
Shapiro, L., and Stockman, G., 2001. Computer Vision. Pearson Education: 608 p.
Smettem, K.R.J., and B.E. Clothier, Measuring unsaturated sorptivity and hydraulic conductivity using multiple disc permeameters, J. Soil Sci., 40, 563–568, 1989.
Soil Moisture Corp. 1987. Model 2800K1 Guelph Permeameter: Operating instructions. Santa Barbara, CA 93105.
Sørensen, K.I., F. Effersø, E. Auken, and L. Pellerin. 2001. HYDR09: An auger tool to estimate hydraulic conductivity. EEGS2001 Proceedings- Hydrogeophysics Session (HYDR): 204-205.
Tan, P., Steinbach, M., and Kumar, V., 2006. Introduction to data mining. Pearson Education: 709 p.
Thomas, S. D., Corbett, P. W. M. & Jensen, J. L. 1997. Upscaling Vertical Permeability within a Fluvio-Aeolian Reservoir. Paper presented at the 4th International Reservoir Characterization Technical Conference, Houston, Texas, 2–4 March.
Valentin C, A. Casenave. 1992. Infiltration Into Sealed Soils as Influenced by Gravel Cover, Soil Sci. Soc. Am. J., 56(6):1667-1673.
Valentin C. 1994. Surface Sealing as Affected by Various Rock Fragment Covers In West-Africa, Catena, 23(1-2): 87-97.
van Genuchten, M. Th. 1980. A closed-form equation for pre- dicting the hydraulic conductivity of unsaturated soils. Soil. Sci. Soc. Am. J. 44:892-898
Wakeman RJ.1975. Packing Densities of Particles with Log-Normal Size Distributions, Powder Technology, 11(3):297-299.
Warrick, A. W., Models for disc infiltrometers, Water Resour. Res., 28, 1319–1327, 1992.
White, I., and M. J. Sully, Macroscopic and microscopic capillary length and time scales from field infiltration, Water Resour. Res., 23, 1514–1522, 1987.
Wooding, R.A. 1968. Steady infiltration from a shallow circular pond. Water Resour. Res. 4:1259-1273.
Wu, L., J. B. Swan, J. L. Nieber, and R. R. Allmaras, Soil-macropore and layer influences on saturated hydraulic conductivity measured with borehole permeameters, Soil Sci. Soc. Am. J., 57, 917–923, 1993.
Yu AB, RP Zhou, and N Standish. 1996a. “Modifying The Linear Packing Model For Predicting The Porosity of Nonspherical Particle Mixtures.” Ind. Eng. Chem. Res. 35:3730–3741.
Yu AB, RP Zou, and N Standish. 1996b. “On The Modelling of The Packing Of Fine Particles.” Powder Technol., 92:185–194.
Yu AB, and N Standish. 1993. “Study of The Packing Of Particles With A Mixture Size Distribution.” Powder Technol., 76(2):113–124.

Zhang, R. 1997. Determination of soil sorptivity and hydraulic conductivity from the disk infiltrometer. Soil Sci. Soc. Am. J. 61:1024-1030.
Zhang, Z.F., P.H. Groenevelt, and G.W. Parkin. 1998. The well-shape factor for the measurement of soil hydraulic properties using the Guelph Permeameter. Soil and Tillage Research, 49(3): 219-221.

Attachment 1: Publications and Presentations

Publications

Seedahmed GH, and AL Ward. 2005. Scale-Space Mutual Information for Textural-Patterns Characterization. ACTA Press. (http://www.Actapress.Com/Paperinfo.Aspx?Paperid=21370)

Presentations

Seedahmed, G.H., A.L. Ward. 2005. Scale-space second moment matrix analysis for textural patterns segmentation and spatial features measurement.

Seedahmed, G.H., and A.L. Ward. 2005. Scale-Space Mutual Information for Textural-Patterns Characterization. International Association of Science and Technology for Development Conference, Hawaii, August 2005.

Seedahmed, G.H., A.L. Ward. 2005. Scale-space second moment matrix analysis for textural patterns segmentation and spatial features measurement. Presented at the SSSA Annual Meeting Nov. 6-10, 2005 Salt Lake City, UT.

Ward, A.L., G.H. Seedahmed, G. Anderson, Z.F. Zhang. 2005. Hydraulic parameter characterization using borehole permeametry and image-based grain size statistics. Presented at the SERDP-ESTCP Symposium, Washington, D.C., Nov. 29- Dec. 1, 2005.

Zhang, Z.F., A.L. Ward, and J. Keller. 2005. Determining the Hydraulic Conductivity of Sediments Containing Gravels. ASA-CSSA-SSSA Annual Meeting Abstracts, Nov. 6-10, 2005, Salt Lake City, Utah.

Ward, A.L., G.H. Seedahmed, and G. Anderson. 2006. Integration of Multi-tension Permeametry and Photogrammetric Textural Segmentation for Estimating Directional Permeability. Presented at the SERDP-ESTCP Symposium, Washington, D.C., Nov. 29- Dec. 1, 2006.

Ward, A.L, and G.H Seedahmed. 2007. Sediment particle size distribution using digital photogrammetry.

Ward, A.L, and G.H Seedahmed. 2007. Hydraulic parameter characterization using borehole permeametry and image-based grain size statistics.

Johnson, BA and AL Ward. 2007. A Portable Toolbox for the Visualization and Processing of Multimodal Geophysical Measurements. New Orleans, August 2007.

Attachment 2: Students

Carter, LaShane. Mechanical Engineering undergraduate (Eastern Washington University), worked for Dr. Andy Ward, Pacific Northwest National Laboratories, summers 2005, 2006.

Chambers, A. Computer Science undergraduate (University of Texas), worked for Dr. Andy Ward, Pacific Northwest National Laboratories, summers 2005, 2006.

Johnson, Bruce. Computer Engineering undergraduate (University of Tennessee – Knoxville), worked for Dr. Gamal Seedahmed, Pacific Northwest National Laboratories, summer 2005.

Johnson, Bruce. Computer Engineering undergraduate (University of Tennessee – Knoxville), worked for Dr. Andy Ward, Pacific Northwest National Laboratories, summers 2006, 2007.

Okembgo, Kaetochi. Chemical Engineering undergraduate (Yale University), worked for Dr. Andy Ward, Pacific Northwest National Laboratories, summers 2006, 2007.

Tillman, Ameer. Mechanical Engineering undergraduate (Washington State University), worked for Dr. Andy Ward, Pacific Northwest National Laboratories, summer 2007.